



ATLAS Note

GROUP-2017-XX

21st January 2021



Draft version 0.1

1

2 WZ + Heavy Flavor Production in pp collisions 3 at $\sqrt{s} = 13 \text{ TeV}$

4

The ATLAS Collaboration

5

A measurement of WZ produced with an associated heavy flavor jet is performed using 140 fb^{-1} of proton-proton collision data at $\sqrt{s} = 13 \text{ TeV}$ from the ATLAS experiment at the LHC. The measurement is performed in the fully leptonic decay mode, $\text{WZ} \rightarrow \ell\bar{\nu}\ell\bar{\nu}$. The cross-section of $\text{WZ} + b\text{-jets}$ is measured to be $X \pm X \pm X$, while the cross-section of $\text{WZ} + c\text{-charm}$ is measured as X , with a correlation of X between the two processes.

6

7

8

9

© 2021 CERN for the benefit of the ATLAS Collaboration.

10 Reproduction of this article or parts of it is allowed as specified in the CC-BY-4.0 license.

11 **Contents**

12	1 Changes and outstanding items	3
13	1.1 Changelog	3
14	1.1.1 Changes relative to v3	3
15	1.1.2 Changes relative to v2	3
16	1.1.3 Changes relative to v1	4
17	1.2 Outstanding Items	4
18	2 Executive Summary	5
19	3 Data and Monte Carlo Samples	5
20	3.1 Data Samples	6
21	3.2 Monte Carlo Samples	6
22	4 Object Reconstruction	7
23	4.1 Trigger	7
24	4.2 Light leptons	7
25	4.3 Jets	8
26	4.4 B-tagged Jets	10
27	4.5 Missing transverse energy	11
28	5 Event Selection and Signal Region Definitions	11
29	5.1 Event Preselection	11
30	5.2 Fit Regions	15
31	5.3 Non-Prompt Lepton Estimation	27
32	5.3.1 $t\bar{t}$ Validation	27
33	5.3.2 Z+jets Validation	31
34	6 tZ Interference Studies and Separation Multivariate Analysis	35
35	6.1 Interference Studies	36
36	6.2 Top Mass Reconstruction	37
37	6.3 tZ BDT	38
38	7 Systematic Uncertainties	41
39	8 Results	44
40	8.1 1-jet Fit Results	45
41	8.2 2-jet Fit Results	51
42	9 Conclusion	55

43 1 Changes and outstanding items

44 1.1 Changelog

45 This is version 4

46 1.1.1 Changes relative to v3

- 47 • Merged introduction into executive summary, including unblinding details and list of
48 SRs/CRs used
- 49 • listed ptag used (p4133), and release (AB 21.2.127)
- 50 • Included table reftab:xsecUnc listing x-sec uncertainties used
- 51 • Removed selection criteria listed in table ?? (QMisID, AmbiguityType) that were removed
52 from the analysis
- 53 • specified variable used to make truth jet flavor determination (HadronConeExclTruthLa-
54 belIID)
- 55 • fixed bug in MtLepMet calculation, updated selection/fits to account for this
- 56 • Included plots of MtLepMet and PtZ, swapped lep 1 and 2 p_T plots for lep W and lep Z
57 plots
- 58 • updated tZ BDT training to reduce overfitting, updated plots to include error bars, feature
59 importance
- 60 • updated table 8 to clarify selection, fix the tZ_BDT cut used
- 61 • replace a few broken ntuples which included large weight events
- 62 • include DL1r distribution for Z+jets and t \bar{t} VRs
- 63 • Expanded section on facts, included information on derived scale factors from VRs.

64 1.1.2 Changes relative to v2

- 65 • Added alternate VBS samples to include missing b-jet diagrams
- 66 • Included a section on tZ interference effects, 6.1.
- 67 • Updated to reflect changes for 2018, including the move to PFlow jets, DL1r, updated
68 trigger, and updated AnalysisBase version (now 21.2.127)
- 69 • Revised fit regions, using separate 1-jet and 2-jet fits, with all 2-j regions included
- 70 • updated plots for tZ BDT, added details about the model

- 71 • Included truth jet information

72 **1.1.3 Changes relative to v1**

- 73 • Added GRL list
74 • Fixed latex issue in line 92, typo in line 172
75 • Added tables 6 and 4, summarizing the event and object selection
76 • Added table 2, which includes the DSID of samples used
77 • Included reference to WZ inclusive paper in introduction

78 **1.2 Outstanding Items**

- 79 • Unblind, update plots and fits to include data
80 • Include truth jet studies
81 • Add cross-section, significance once unblinded

82 2 Executive Summary

83 The production of WZ in association with a heavy flavor jet represents an important background
 84 for many major analyses. This includes any process with leptons and b-jets in the final state,
 85 such as $t\bar{t}H$, $t\bar{t}W$, and $t\bar{t}Z$. While precise measurements have been made of WZ production
 86 [1], $WZ +$ heavy flavor remains poorly understood. This is largely because the QCD processes
 87 involved in the production of the b-jet make it difficult to simulate accurately. This introduces a
 88 large uncertainty for analyses that include this process as a background.

89 Motivated by its relevance to the $t\bar{t}H$ multilepton analysis, we perform a study of the fully
 90 leptonic decay mode of this channel; that is, events where both the W and Z decay leptonically.
 91 Because WZ has no associated jets at leading order, while the major backgrounds for this channel
 92 tend to have high jet multiplicity, events with more than two jets are rejected. This gives a final
 93 state signature of three leptons and one or two jets.

94 Events that meet this selection criteria are sorted into pseudo-continuous b-tagging regions based
 95 on the DL1r b-tag score of their associated jets. This is done to separate $WZ +$ b-jet events
 96 from $WZ +$ charm and $WZ +$ light jets. These orthogonal categories, in addition to a tZ Control
 97 Region formed using an MVA, are the Signal Regions for the analysis. These regions are fit to
 98 data in order make a more accurate estimate of the contribution of $WZ +$ heavy-flavor, where
 99 heavy-flavor jets include b-jets and charm jets. Separate fits are performed for 1-jet and 2-jet
 100 events. The full Run-2 dataset collected by the ATLAS detector, representing 139 fb^{-1} of data
 101 from pp collisions at $\sqrt{s} = 13 \text{ TeV}$, is used for this study.

102 All backgrounds are accounted for using Monte Carlo, with the simulation of non-prompt lepton
 103 backgrounds - $Z+jets$ and $t\bar{t}$ - validated using non-prompt Validation Regions.

104 Section 3 details the data and Monte Carlo (MC) samples used in the analysis. The reconstruction
 105 of various physics objects is described in section 4. Section 5 describes the event selection applied
 106 to these samples, along the definitions of the various regions used in the fit. The multivariate
 107 analysis techniques used to separate the tZ background from $WZ +$ heavy flavor are described in
 108 section 6. Section 7 describes the various sources of systematic uncertainties considered in the
 109 fit. Finally, the results of the analysis are summarized in section 8, followed by a brief conclusion
 110 in section 9.

111 The current state of the analysis shows blinded results for the full 2018 dataset. Regions containing
 112 $>5\%$ $WZ+b$ events are blinded, and results are from Asimov, MC only fits. In addition to adding
 113 some additional information to this note, remaining tasks include performing WZ/tZ interference
 114 studies, finalizing the presentation of results, and unblinding.

115 3 Data and Monte Carlo Samples

116 Both data and Monte Carlo samples used in this analysis were prepared in the xAOD format,
 117 which was used to produce a Dx AOD sample in the HIGG8D1 derivation framework. The HIGG8D1

118 framework is designed for the $t\bar{t}H$ multi-lepton analysis, which targets events with multiple
 119 leptons as well as tau hadrons. This framework skims the dataset to remove unneeded variables
 120 as well as entire events. Events are removed from the derivations that do not meet the following
 121 selection:

- 122 • at least two light leptons within a range $|\eta| < 2.6$, with leading lepton $p_T > 15$ GeV and
 123 subleading lepton $p_T > 5$ GeV
- 124 • at least one light lepton with $p_T > 15$ GeV within a range $|\eta| < 2.6$, and at least two hadronic
 125 taus with $p_T > 15$ GeV.

126 Samples were then generated from these HIGG8D1 derivations with p-tag of p4134 using a
 127 modified version of AnalysisBase version 21.2.127.

128 3.1 Data Samples

129 The study uses a sample of proton-proton collision data collected by the ATLAS detector from
 130 2015 through 2018 at an energy of $\sqrt{s} = 13$ TeV, which represents an integrated luminosity of
 131 139 fb^{-1} . This data set was collected with a bunch crossing rate of 25 ns. All data used in this
 132 analysis was verified by data quality checks, having been included in the following Good Run
 133 Lists:

- 134 • data15_13TeV.periodAllYear_DetStatus-v79-repro20-02_DQDefects-00-02-02
 135 _PHYS_StandardGRL_All_Good_25ns.xml
- 136 • data16_13TeV.periodAllYear_DetStatus-v88-pro20-21_DQDefects-00-02-04
 137 _PHYS_StandardGRL_All_Good_25ns.xml
- 138 • data17_13TeV.periodAllYear_DetStatus-v97-pro21-13_Unknown_PHYS_StandardGRL
 139 _All_Good_25ns_Triggerno17e33prim.xml
- 140 • data18_13TeV.periodAllYear_DetStatus-v102-pro22-04_Unknown_PHYS_StandardGRL
 141 _All_Good_25ns_Triggerno17e33prim.xml

142 Runs included from the AllYear period containers are included.

143 3.2 Monte Carlo Samples

144 Several different generators were used to produce Monte Carlo simulations of the signal and
 145 background processes. For all samples, the response of the ATLAS detector is simulated using
 146 Geant4. The WZ signal samples are simulated using Sherpa 2.2.2 [2]. Specific information
 147 about the Monte Carlo samples being used can be found in table 1. A list of the specific samples
 148 used by data set ID is shown in table 2.

Table 1: The configurations used for event generation of signal and background processes, including the event generator, matrix element (ME) order, parton shower algorithm, and parton distribution function (PDF).

Process	Event generator	ME order	Parton Shower	PDF
WZ, VV	SHERPA 2.2.2	MEPS NLO	SHERPA	CT10
tZ	MG5_AMC	LO	PYTHIA 6	CTEQ6L1
t̄W	MG5_AMC (SHERPA 2.1.1)	NLO (LO multileg)	PYTHIA 8 (SHERPA)	NNPDF 3.0 NLO (NNPDF 3.0 NLO)
t̄(Z/γ* → ll)	MG5_AMC	NLO	PYTHIA 8	NNPDF 3.0 NLO
t̄H	MG5_AMC (MG5_AMC)	NLO (NLO)	PYTHIA 8 (HERWIG++)	NNPDF 3.0 NLO [Ball:2014uwa] (CT10 [ct10])
tHqb	MG5_AMC	LO	PYTHIA 8	CT10
tHW	MG5_AMC (SHERPA 2.1.1)	NLO (LO multileg)	HERWIG++ (SHERPA)	CT10 (NNPDF 3.0 NLO)
tWZ	MG5_AMC	NLO	PYTHIA 8	NNPDF 2.3 LO
t̄t, t̄t̄t̄	MG5_AMC	LO	PYTHIA 8	NNPDF 2.3 LO
t̄W+W-	MG5_AMC	LO	PYTHIA 8	NNPDF 2.3 LO
t̄t	Powheg-BOX v2 [powheggtt]	NLO	PYTHIA 8	NNPDF 3.0 NLO
t̄t̄γ	MG5_AMC	LO	PYTHIA 8	NNPDF 2.3 LO
s-, t-channel, Wt single top	Powheg-BOX v1 [powhegstp]	NLO	PYTHIA 6	CT10
qqVV, VVV Z → l+l-	SHERPA 2.2.1	MEPS NLO	SHERPA	NNPDF 3.0 NLO

4 Object Reconstruction

All regions defined in this analysis share a common lepton, jet, and overall event preselection. The selection applied to each physics object is detailed here; the event preselection, and the selection used to define the various fit regions, is described in section 5.

4.1 Trigger

Events are required to be selected by dilepton triggers, as summarized in table 3.

4.2 Light leptons

Electron candidates are reconstructed from energy clusters in the electromagnetic calorimeter that are associated with charged particle tracks reconstructed in the inner detector [3]. Electron candidates are required to have $p_T > 10$ GeV and $|\eta_{\text{cluster}}| < 2.47$. Candidates in the transition region between different electromagnetic calorimeter components, $1.37 < |\eta_{\text{cluster}}| < 1.52$, are rejected. A multivariate likelihood discriminant combining shower shape and track information is used to distinguish real electrons from hadronic showers (fake electrons). To further reduce

Sample	DSID
WZ	364253, 364739-42
VV	364250, 364254, 364255, 363355-60, 364890
t̄W	410155
t̄Z	410156, 410157, 410218-20
low mass t̄Z	410276-8
Rare Top	410397, 410398, 410399
single Top	410658-9, 410644-5
three Top	304014
four Top	410080
t̄WW	410081
Z + jets	364100-41
low mass Z + jets	364198-215
W + jets	364156-97
Vγ	364500-35
tZ	410560
tW	410013-4
WtZ	410408
VVV	364242-9
VH	342284-5
WtH	341998
t̄tγ	410389
t̄t	410470
t̄tH	345873-5, 346343-5

Table 2: List of Monte Carlo samples by data set ID used in the analysis.

162 the non-prompt electron contribution, the track is required to be consistent with originating from
 163 the primary vertex; requirements are imposed on the transverse impact parameter significance
 164 ($|d_0|/\sigma_{d_0}$) and the longitudinal impact parameter ($|\Delta z_0 \sin \theta_\ell|$), as shown in table 4.

165 Muon candidates are reconstructed by combining inner detector tracks with track segments or
 166 full tracks in the muon spectrometer [4]. Muon candidates are required to have $p_T > 10$ GeV
 167 and $|\eta| < 2.5$.

168 All leptons are required to be isolated, and pass a non-prompt BDT selection described in detail
 169 in [5].

170 4.3 Jets

171 Jets are reconstructed from calibrated topological clusters built from energy deposits in the
 172 calorimeters [6], using the anti- k_t algorithm with a radius parameter $R = 0.4$. Jets with energy
 173 contributions likely arising from noise or detector effects are removed from consideration [7],

Dilepton triggers (2015)		
$\mu\mu$ (asymm.)	HLT_mu18_mu8noL1	
ee (symm.)	HLT_2e12_lhloose_L12EM10VH	
$e\mu, \mu e$ (\sim symm.)	HLT_e17_lhloose_mu14	
Dilepton triggers (2016)		
$\mu\mu$ (asymm.)	HLT_mu22_mu8noL1	
ee (symm.)	HLT_2e17_lhvloose_nod0	
$e\mu, \mu e$ (\sim symm.)	HLT_e17_lhloose_nod0_mu14	
Dilepton triggers (2017)		
$\mu\mu$ (asymm.)	HLT_mu22_mu8noL1	
ee (symm.)	HLT_2e24_lhvloose_nod0	
$e\mu, \mu e$ (\sim symm.)	HLT_e17_lhloose_nod0_mu14	
Dilepton triggers (2018)		
$\mu\mu$ (asymm.)	HLT_mu22_mu8noL1	
ee (symm.)	HLT_2e24_lhvloose_nod0	
$e\mu, \mu e$ (\sim symm.)	HLT_e17_lhloose_nod0_mu14	

Table 3: List of lowest p_T -threshold, un-prescaled dilepton triggers used for 2015-2018 data taking.

	e			μ						
	L	L^*	T	L	L^*	T				
FixedCutLoose	No	Yes		No	Yes					
Non-prompt lepton BDT	No	Yes		No	Yes					
Identification	Loose	Tight		Loose	Medium					
Transverse impact parameter significance $ d_0 /\sigma_{d_0}$	< 5			< 3						
Longitudinal impact parameter $ z_0 \sin \theta $	< 0.5 mm									

Table 4: Loose (L), loose and minimally-isolated (L^*), and tight (T) light lepton definitions.

and only jets satisfying $p_T > 25$ GeV and $|\eta| < 2.5$ are used in this analysis. For jets with $p_T < 60$ GeV and $|\eta| < 2.4$, a jet-track association algorithm is used to confirm that the jet originates from the selected primary vertex, in order to reject jets arising from pileup collisions [8].

178 **4.4 B-tagged Jets**

179 In order to make a measurement of $WZ +$ heavy flavor it is necessary to distinguish these events
 180 from $WZ +$ light jets. For this purpose, the DL1r b-tagging algorithm is used to distinguish
 181 heavy flavor jets from lighter ones. The DL1r algorithm uses jet kinematics, particularly jet
 182 vertex information, as input for a neural network which assigns each jet a score designed to
 183 reflect how likely that jet is to have originated from a b-quark.

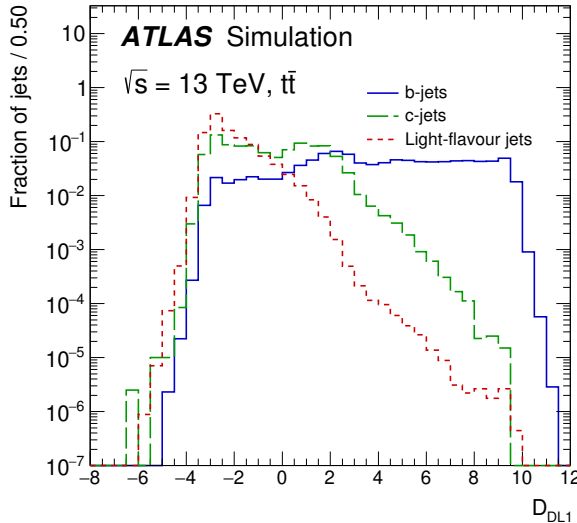


Figure 1: Output distribution of the DL1r algorithm for b-jets, charm jets, and light jets

184 From the output of the BDT, working points (WPs) are developed based on the efficiency of truth
 185 b-jets at particular values of the DL1r algorithm. The working points used in this analysis are
 186 summarized in table 5.

WP	none	loose	medium	tight	tightest
b eff.	-	85%	77%	70%	60%

Table 5: B-tagging Working Points by tightness and b-jet efficiency

187 A tighter WP will accept fewer b-jets, but reject a higher fraction of charm and light jets.
 188 Generally, analyses that include b-jets will use a fixed working point, for example, requiring that
 189 a jet pass the 70% threshold. By instead treating these working point as bins, e.g. events with
 190 jets that fall between the 85% and 77% WPs fall into one bin, while events with jets passing the
 191 60% WP fall into another, and looking at the full psuedo-continuous DL1r spectrum of the jets,
 192 additional information can be gained. The psuedo-continuous b-tag spectrum is used in this case
 193 to separate out $WZ + b$, $WZ + \text{charm}$, and $WZ + \text{light}$.

194 **4.5 Missing transverse energy**

195 Missing transverse momentum (E_T^{miss}) is used as part of the event selection. The missing
 196 transverse momentum vector is defined as the inverse of the sum of the transverse momenta of
 197 all reconstructed physics objects as well as remaining unclustered energy, the latter of which is
 198 estimated from low- p_T tracks associated with the primary vertex but not assigned to a hard object,
 199 with object definitions taken from [9]. Light leptons considered in the E_T^{miss} reconstruction are
 200 required to have $p_T > 10$ GeV, while jets are required to have $p_T > 20$ GeV.

201 **5 Event Selection and Signal Region Definitions**

202 Event are required to pass a preselection described in section 5.1 and summarized in table 6.
 203 Those that pass this preselection are divided into various fit regions described in section 5.2,
 204 based on the number of jets in the event, and the b-tag score of those jets.

205 **5.1 Event Preselection**

206 Events are required to include exactly three reconstructed light leptons passing the requirement
 207 described in 4.2, which have a total charge of ± 1 . As the opposite sign lepton is found to
 208 be prompt the vast majority of the time [5], it is required to be loose and isolated, as defined
 209 though the standard `isolationFixedCutLoose` working point supported by combined per-
 210 formance groups. The same sign leptons are required to be very tight, as per the recommended
 211 `isolationFixedCutTight`.

212 The leptons are ordered in the analysis code as 0, 1, and 2. Lepton 0 is the lepton whose charge
 213 is opposite the other two. Lepton 1 is the lepton closest to the opposite charge lepton, i.e. the
 214 smallest ΔR , leaving lepton 2 as the lepton further from the opposite charge lepton. Lepton 0
 215 is required to have $p_T > 10$ GeV, while the same sign leptons, 1 and 2, are required to have
 216 $p_T > 20$ GeV to reduce the contribution of non-prompt leptons.

217 The invariant mass of at least one pair of opposite sign, same flavor leptons is required to fall
 218 within 10 GeV of the mass of the Z boson, 91.2 GeV. Events where one of the opposite sign pairs
 219 have an invariant mass less than 12 GeV are rejected in order to suppress low mass resonances.

220 An additional requirement is placed on the missing transverse energy, $E_T^{\text{miss}} > 20$ GeV, and the
 221 transverse mass of the W candidate, $m(E_T^{\text{miss}} + l_{\text{other}}) > 30$ GeV, where E_T^{miss} is the missing
 222 transverse energy, and l_{other} is the lepton not included in the Z-candidate.

223 Events are required to have one or two reconstructed jets passing the selection described in
 224 section 4.3. Events with more than two jets are rejected in order to reduce the contribution of
 225 backgrounds such as $t\bar{t}Z$ and $t\bar{t}W$, which tend to have higher jet multiplicity.

Event Selection
Exactly three leptons with charge ± 1
Two same-charge leptons with $p_T > 20 \text{ GeV}$
One opposite charge lepton with $p_T > 10 \text{ GeV}$
$m(l^+l^-)$ within 10 GeV of 91.2 GeV
Transverse mass of W-candidate, $m_T(E_T^{\text{miss}} + \text{lep}_{\text{other}}) > 30 \text{ GeV}$
Missing transverse energy, $E_T^{\text{miss}} > 20 \text{ GeV}$
One or two jets with $p_T > 25 \text{ GeV}$

Table 6: Summary of the selection applied to events for inclusion in the fit

226 The event yields in the preselection region for both data and Monte Carlo are summarized in
 227 table 5.1, which shows good agreement between data and Monte Carlo, and demonstrates that
 228 this region consists primarily of WZ events. The WZ events are split into WZ + b, WZ + c, and
 229 WZ + 1 based on the truth flavor of the heaviest associated jet in the event. Specifically, this
 230 determination is made based on the HadronConeExclTruthLabelID of the jet. That is, WZ +
 231 1 events contain no charm and b jets at truth level, WZ + c contain at least one truth charm and
 232 no b-jets, and WZ + b contains at least one truth b-jet.

Process	Events
$WZ + b$	167.64 ± 6.45
$WZ + c$	1080.91 ± 39.28
$WZ + l$	7223.37 ± 312.53
Other VV	849.79 ± 142.13
$t\bar{t}W$	16.81 ± 2.31
$t\bar{t}Z$	114.68 ± 17.40
rare Top	2.20 ± 0.14
Single top	0.10 ± 0.45
Three top	0.01 ± 0.01
Four top	0.02 ± 0.01
$t\bar{t}WW$	0.23 ± 0.05
$Z + \text{jets}$	601.16 ± 260.13
$V + \gamma$	36.51 ± 54.34
tZ	194.64 ± 65.74
tW	5.49 ± 1.24
WtZ	25.80 ± 1.07
VVV	26.21 ± 0.87
VH	94.34 ± 7.35
$t\bar{t}$	107.68 ± 8.14
$t\bar{t}H$	4.28 ± 0.46
Total	10556.8 ± 533.4
Data	10574

Table 7: Events yields in the preselection region at 138.9 fb^{-1}

²³³ Here Other VV represents diboson processes other than WZ, and consists predominantly of
²³⁴ $ZZ \rightarrow ll\bar{l}\bar{l}$ events where one of the leptons is not reconstructed.

²³⁵ Simulations are further validated by comparing the kinematic distributions of the Monte Carlo
²³⁶ with data, which are shown in figures 2. Here, bins with 5% or more WZ+b are blinded.

WZ Fit Region - Inclusive

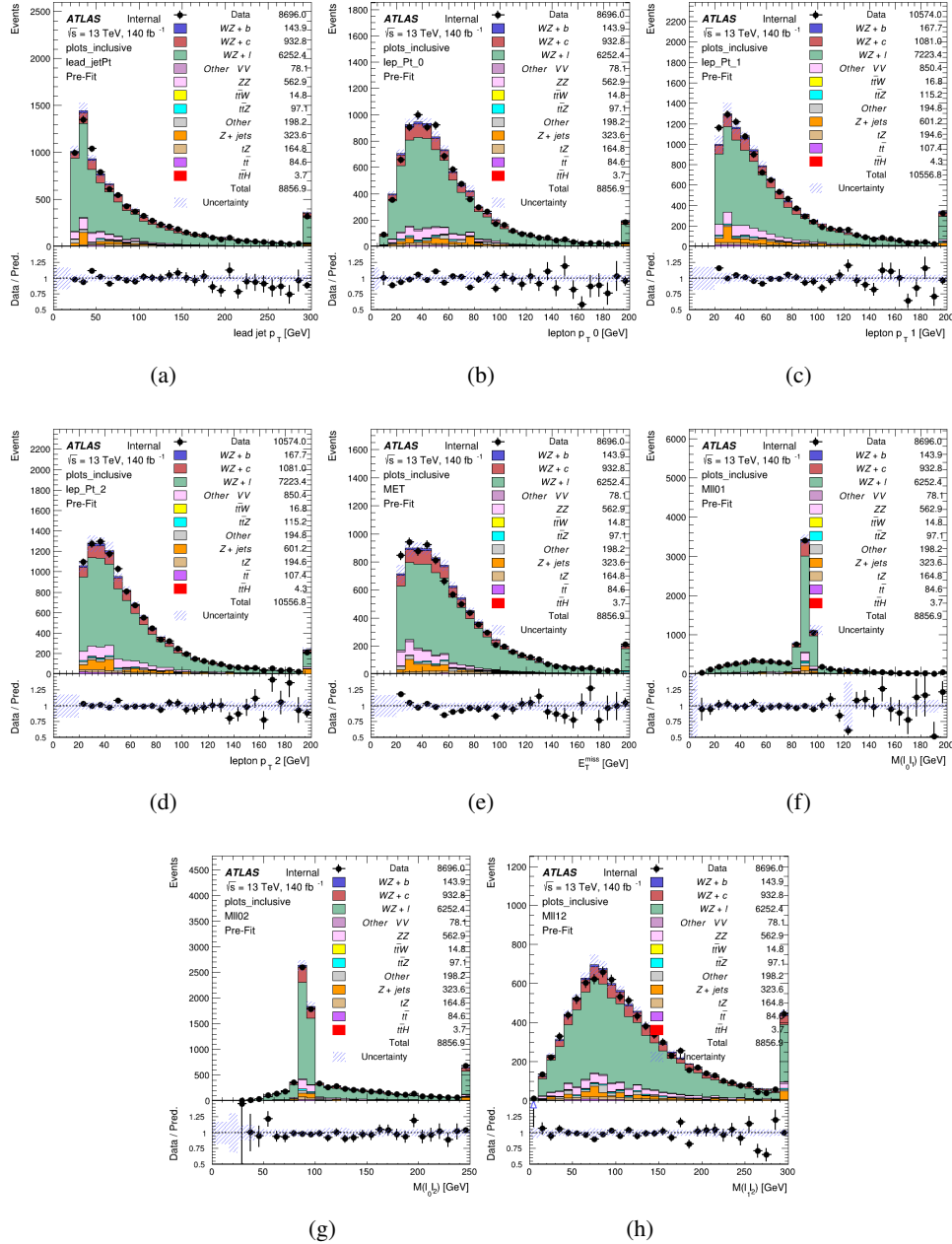


Figure 2: Comparisons between data and MC distributions in the preselection region for the p_T of (a) the leading jet, (b) lepton 0, (c) lepton 1, (d) lepton 2, (e) the missing transverse energy, and (f) the invariant mass of leptons 0 and 1, (g) the invariant mass of leptons 0 and 2, and (h) the invariant mass of leptons 1 and 2.

²³⁷ **5.2 Fit Regions**

²³⁸ Once preselection has been applied, the remaining events are categorized into one of twelve
²³⁹ orthogonal regions. The regions used in the fit are summarized in table 8.

Table 8: A list of the regions used in the fit and the selection used for each.

Region	Selection
1j, <85%	$N_{\text{jets}} = 1, \text{nJets_DL1r_85} = 0$
1j, 85%-77%	$N_{\text{jets}} = 1, \text{nJets_DL1r_85} = 1, \text{nJets_DL1r_77} = 0$
1j, 77%-70%	$N_{\text{jets}} = 1, \text{nJets_DL1r_77} = 1, \text{nJets_DL1r_70} = 0$
1j, 70%-60%	$N_{\text{jets}} = 1, \text{nJets_DL1r_70} = 1, \text{nJets_DL1r_60} = 0$
1j, >60%	$N_{\text{jets}} = 1, \text{nJets_DL1r_60} = 1, tZ \text{ BDT} > 0.725$
1j tZ CR	$N_{\text{jets}} = 1, \text{nJets_DL1r_60} = 1, tZ \text{ BDT} < 0.725$
2j, <85%	$N_{\text{jets}} = 2, \text{nJets_DL1r_85} = 0$
2j, 85%-77%	$N_{\text{jets}} = 2, \text{nJets_DL1r_85} \geq 1, \text{nJets_DL1r_77} = 0$
2j, 77%-70%	$N_{\text{jets}} = 2, \text{nJets_DL1r_77} \geq 1, \text{nJets_DL1r_70} = 0$
2j, 70%-60%	$N_{\text{jets}} = 2, \text{nJets_DL1r_70} \geq 1, \text{nJets_DL1r_60} = 0$
2j, >60%	$N_{\text{jets}} = 2, \text{nJets_DL1r_60} \geq 1, tZ \text{ BDT} > 0.725$
2j tZ CR	$N_{\text{jets}} = 2, \text{nJets_DL1r_60} \geq 1, tZ \text{ BDT} < 0.725$

²⁴⁰ The working points discussed in section 4.4 are used to separate events into fit regions based on
²⁴¹ the highest working point reached by a jet in each event. Because the background composition
²⁴² differs significantly based on the number of b-jets, events are further subdivided into 1 jet and 2
²⁴³ jet regions in order to minimize the impact of background uncertainties.

²⁴⁴ An additional tZ control region is created based on the BDT described in section 6. The region
²⁴⁵ with 1-jet passing the 60% working point is split in two - a signal enriched region of events with
²⁴⁶ a BDT score greater than 0.03, and a tZ control region including events with less than 0.03. This
²⁴⁷ cutoff is arrived at by performing an Asimov fit with a variety of cutoffs, and selecting the value
²⁴⁸ that produces the highest significance for the measurement of WZ + b.

²⁴⁹ The modeling in each region is validated by comparing data and MC predictions for various
²⁵⁰ kinematic distributions. These plot are shown in figures 3-14.

WZ Fit Region - 1j < 85% WP

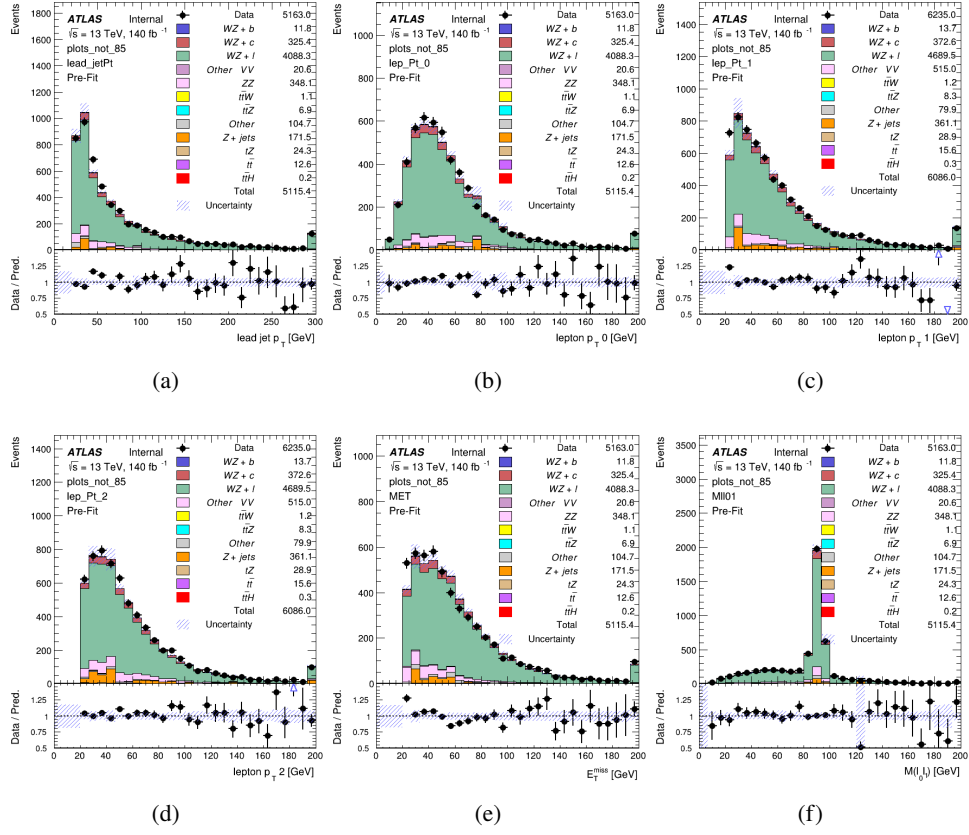


Figure 3: Comparisons between the data and MC distributions in the preselection region for the p_T of (a) the leading jet, (b) lepton 0, (c) lepton 1, (d) lepton 2, (e) the missing transverse energy, and (f) the invariant mass of lepton 0 and 1.

WZ Fit Region - 1j 77-85% WP

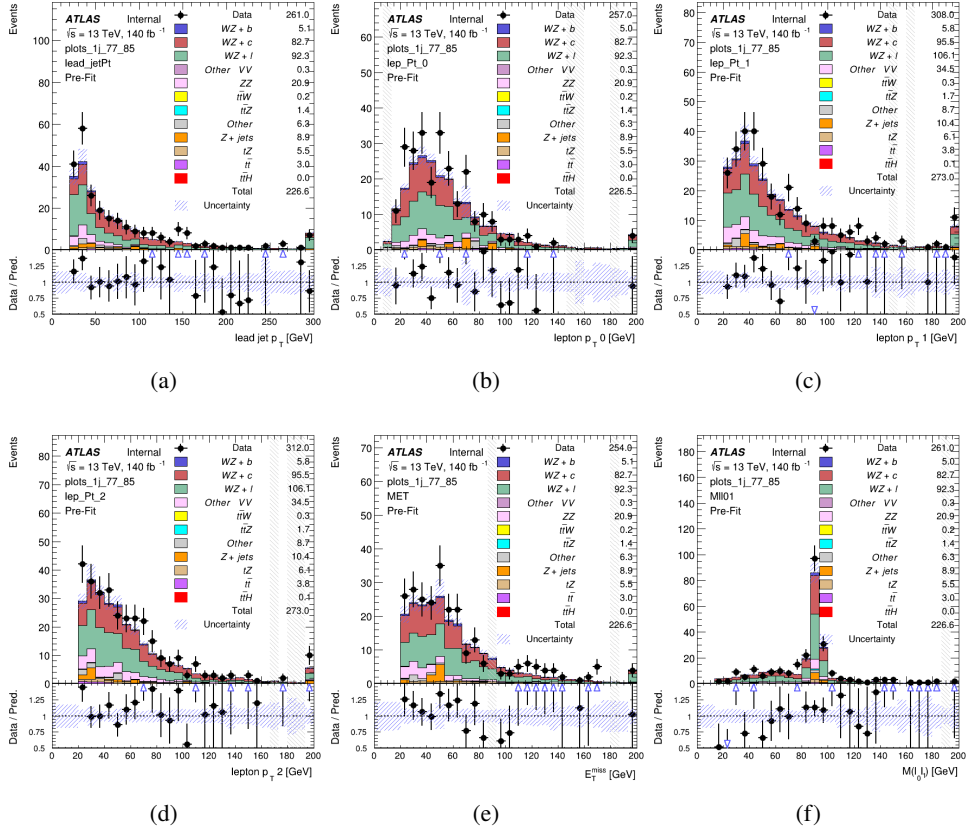


Figure 4: Comparisons between the data and MC distributions in the preselection region for the p_T of (a) the leading jet, (b) lepton 0, (c) lepton 1, (d) lepton 2, (e) the missing transverse energy, and (f) the invariant mass of lepton 0 and 1.

WZ Fit Region - 1j 70-77% WP

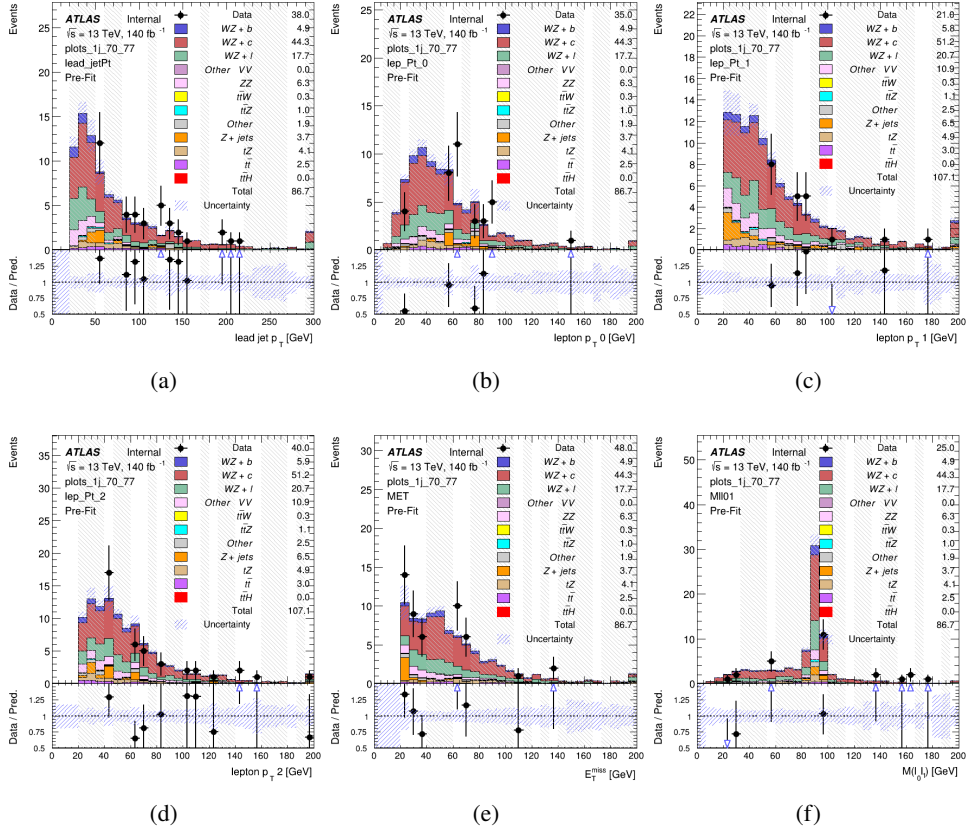


Figure 5: Comparisons between the data and MC distributions in the preselection region for the p_T of (a) the leading jet, (b) lepton 0, (c) lepton 1, (d) lepton 2, (e) the missing transverse energy, and (f) the invariant mass of lepton 0 and 1.

WZ Fit Region - 1j 60-70% WP

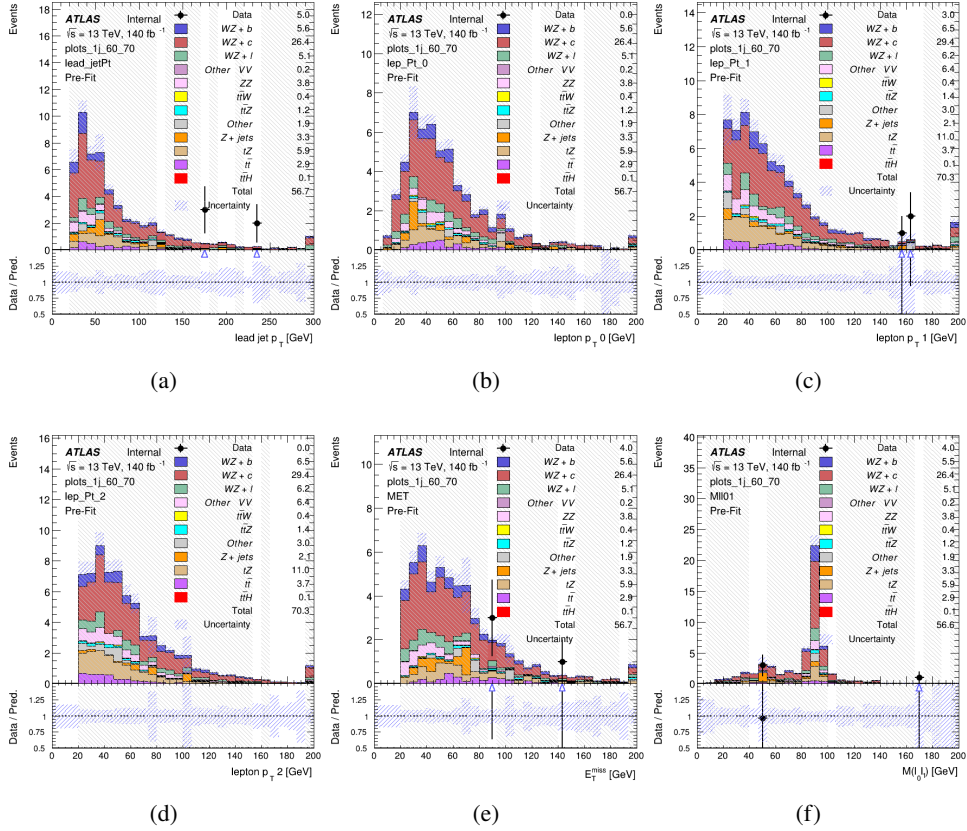


Figure 6: Comparisons between the data and MC distributions in the preselection region for the p_T of (a) the leading jet, (b) lepton 0, (c) lepton 1, (d) lepton 2, (e) the missing transverse energy, and (f) the invariant mass of lepton 0 and 1.

WZ Fit Region - 1j 60% WP

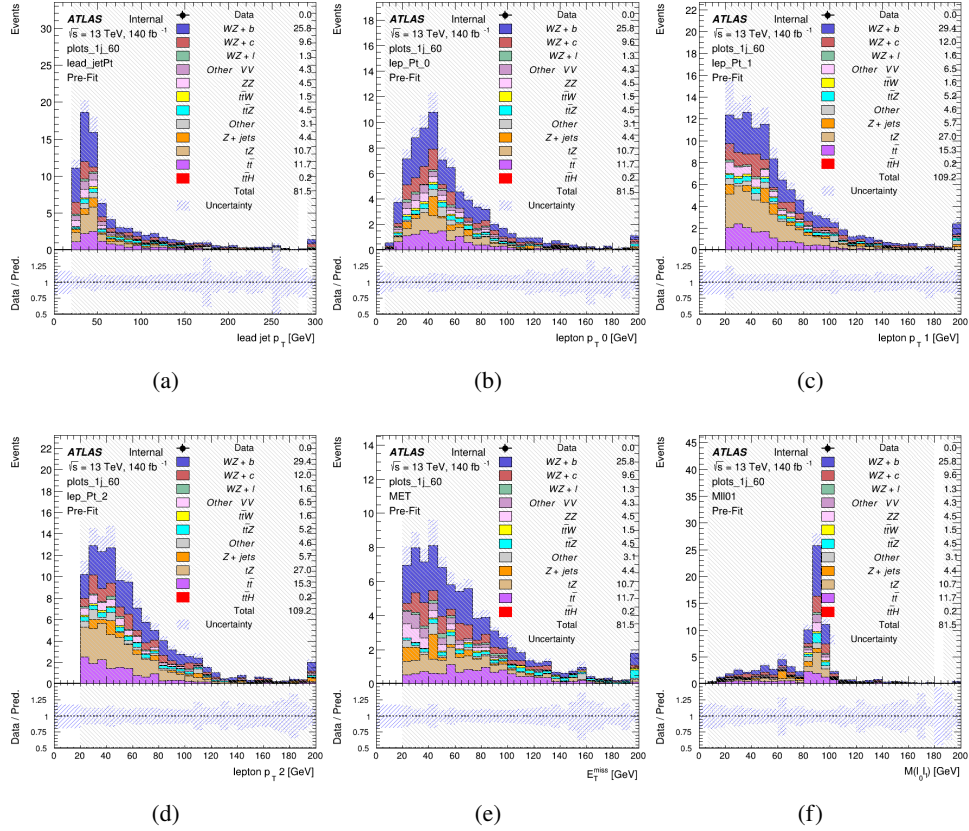


Figure 7: Comparisons between the data and MC distributions in the preselection region for the p_T of (a) the leading jet, (b) lepton 0, (c) lepton 1, (d) lepton 2, (e) the missing transverse energy, and (f) the invariant mass of lepton 0 and 1.

WZ Fit Region - tZ-CR

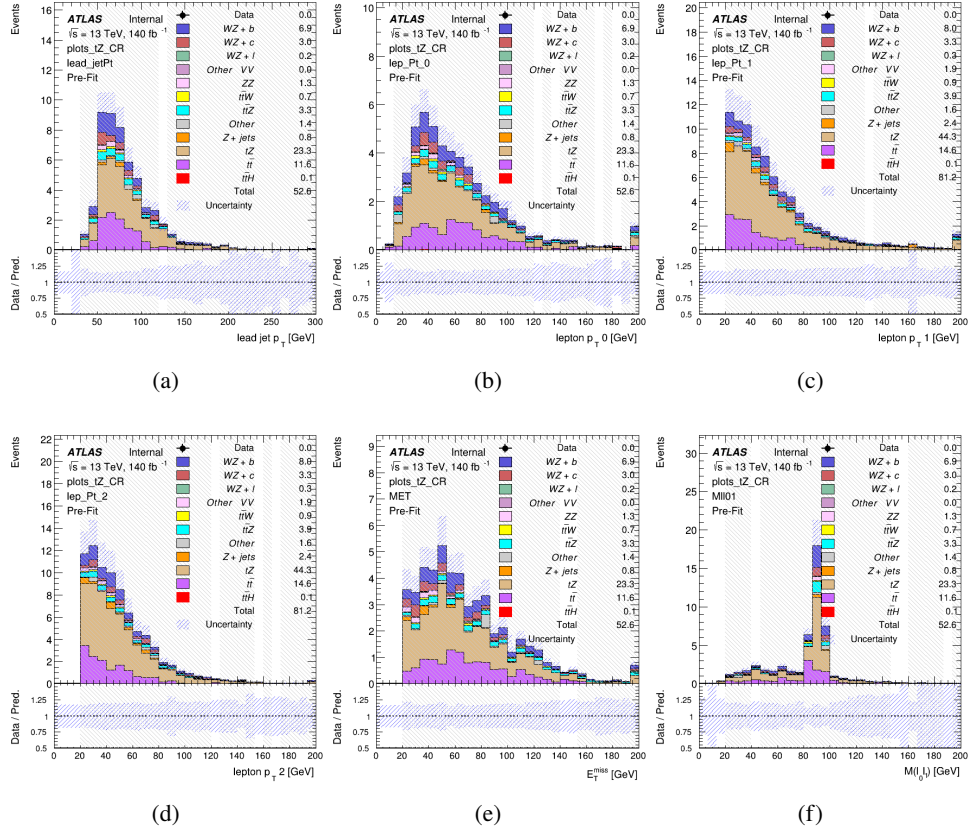


Figure 8: Comparisons between the data and MC distributions in the preselection region for the p_T of (a) the leading jet, (b) lepton 0, (c) lepton 1, (d) lepton 2, (e) the missing transverse energy, and (f) the invariant mass of lepton 0 and 1.

WZ Fit Region - 2j < 85% WP

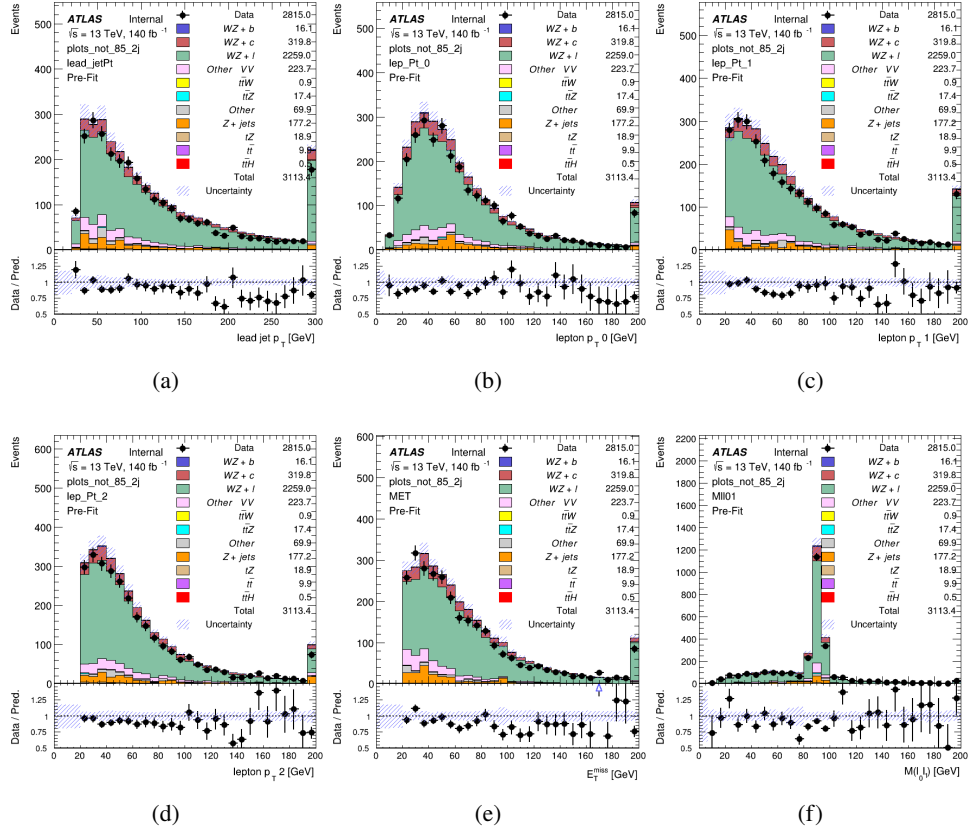


Figure 9: Comparisons between the data and MC distributions in the preselection region for the p_T of (a) the leading jet, (b) lepton 0, (c) lepton 1, (d) lepton 2, (e) the missing transverse energy, and (f) the invariant mass of lepton 0 and 1.

WZ Fit Region - 2j 77-85% WP

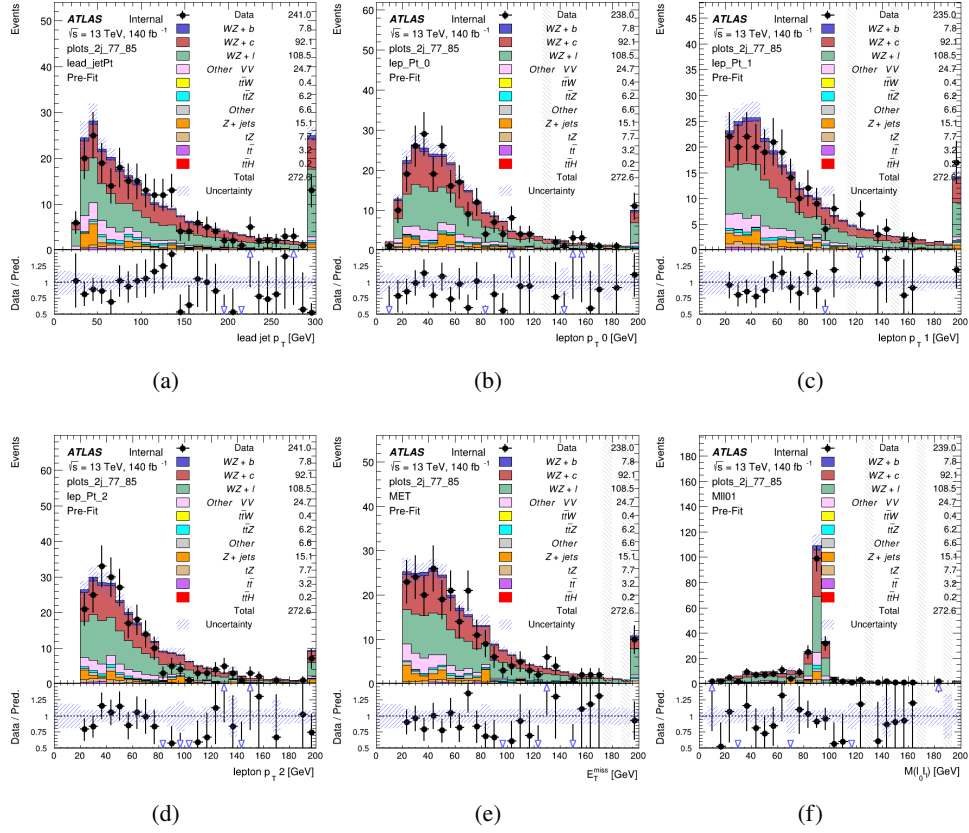


Figure 10: Comparisons between the data and MC distributions in the preselection region for the p_T of (a) the leading jet, (b) lepton 0, (c) lepton 1, (d) lepton 2, (e) the missing transverse energy, and (f) the invariant mass of lepton 0 and 1.

WZ Fit Region - 2j 70-77% WP

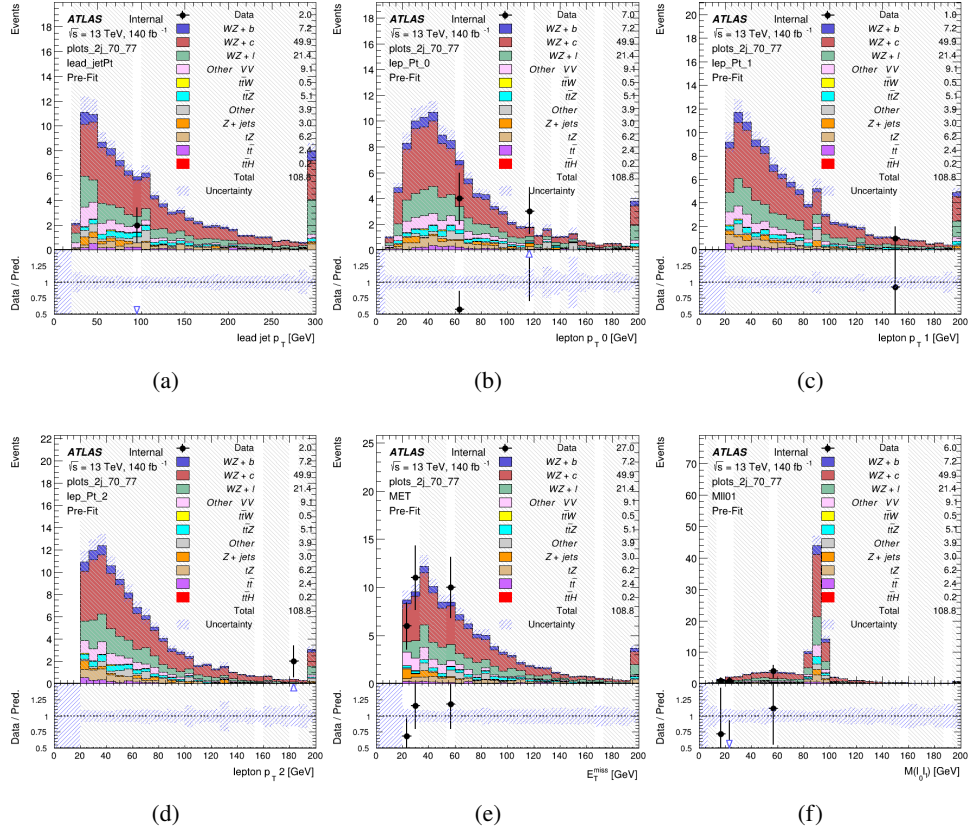


Figure 11: Comparisons between the data and MC distributions in the preselection region for the p_T of (a) the leading jet, (b) lepton 0, (c) lepton 1, (d) lepton 2, (e) the missing transverse energy, and (f) the invariant mass of lepton 0 and 1.

WZ Fit Region - 2j 60-70% WP

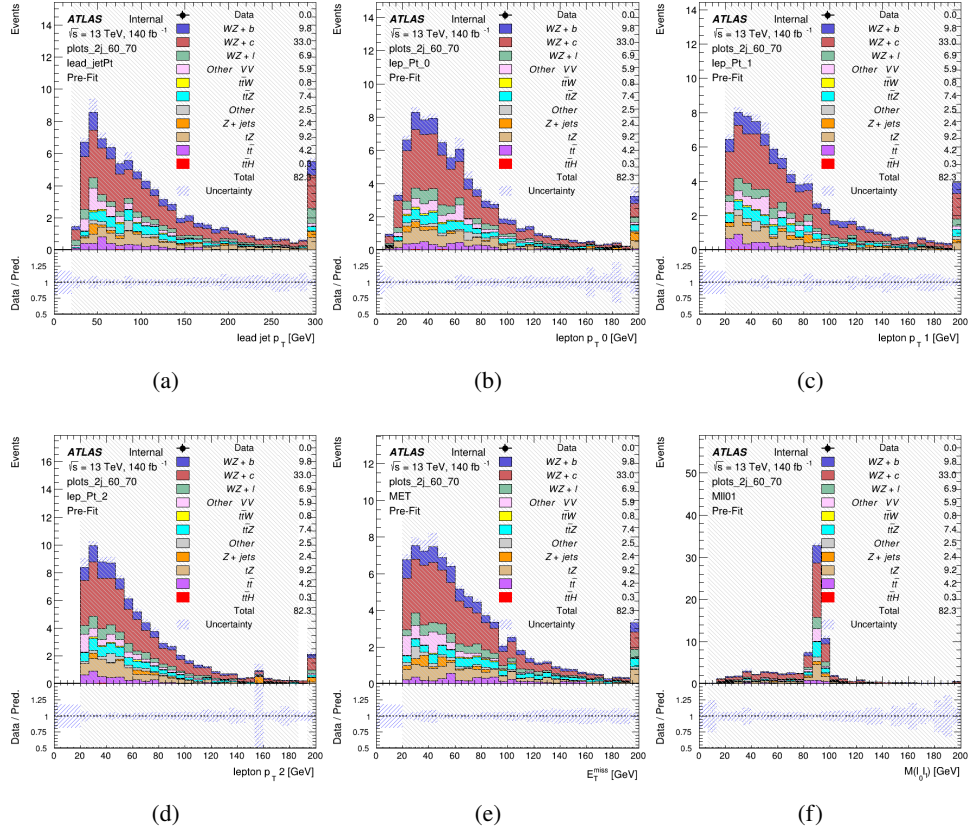


Figure 12: Comparisons between the data and MC distributions in the preselection region for the p_T of (a) the leading jet, (b) lepton 0, (c) lepton 1, (d) lepton 2, (e) the missing transverse energy, and (f) the invariant mass of lepton 0 and 1.

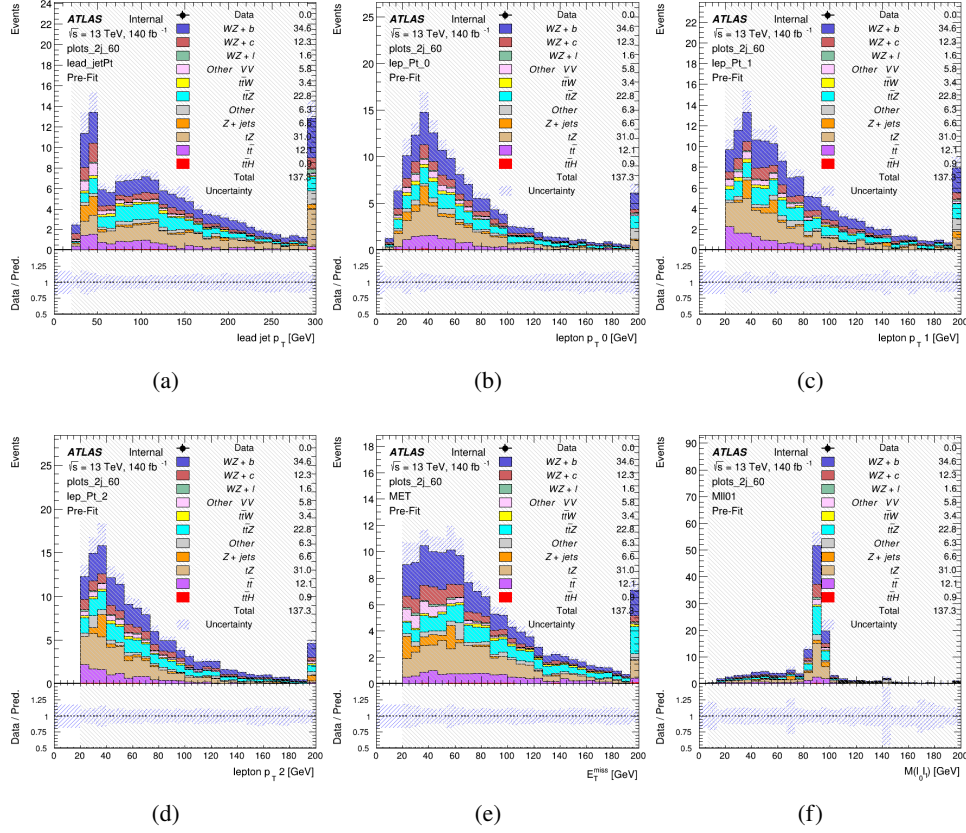
WZ Fit Region - 2j 60% WP

Figure 13: Comparisons between the data and MC distributions in the preselection region for the p_T of (a) the leading jet, (b) lepton 0, (c) lepton 1, (d) lepton 2, (e) the missing transverse energy, and (f) the invariant mass of lepton 0 and 1.

WZ Fit Region - tZ-CR-2j

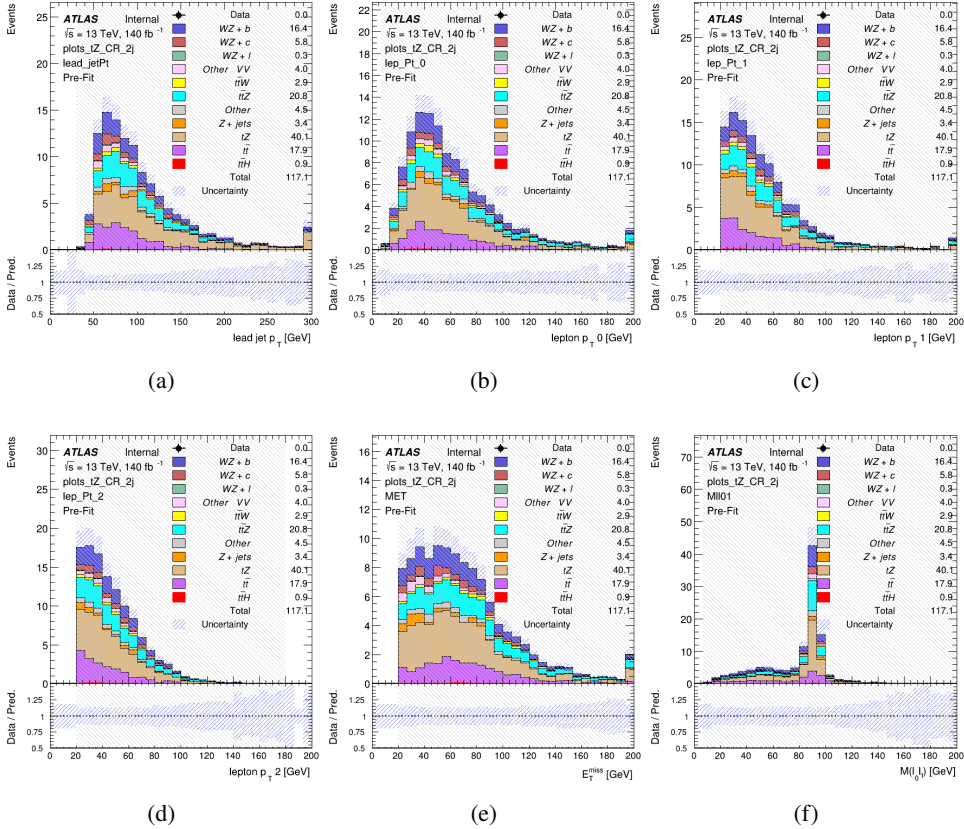


Figure 14: Comparisons between the data and MC distributions in the preselection region for the p_T of (a) the leading jet, (b) lepton 0, (c) lepton 1, (d) lepton 2, (e) the missing transverse energy, and (f) the invariant mass of lepton 0 and 1.

5.3 Non-Prompt Lepton Estimation

Two processes act as sources of non-prompt leptons appear in the analysis: $t\bar{t}$ and $Z+jet$ production both produce two prompt leptons, and each contribute to the 3l region when an additional non-prompt lepton appears in the event. The contribution of these processes is estimated with Monte Carlo simulations, which are validated using enriched validation regions.

5.3.1 $t\bar{t}$ Validation

$t\bar{t}$ events can produce two prompt leptons from the decay of each of the tops. These top decays produce two b-quarks, the decay of which can produce additional non-prompt leptons, which occasionally pass the event preselection. In order to validate that the Monte Carlo accurately

260 simulates this process accurately, the MC prediction in a non-prompt $t\bar{t}$ enriched validation
261 region is compared to data.

262 The $t\bar{t}$ validation region is similar to the preselection region - three leptons meeting the criteria
263 described in section 5 are required, and the requirements on E_T^{miss} remain the same. However,
264 the selection requiring a lepton pair form a Z-candidate are reversed. Events where the invariant
265 mass of any two opposite sign, same flavor leptons falls within 10 GeV of 91.2 GeV are rejected.
266 This ensures the $t\bar{t}$ validation region is orthogonal to the preselection region.

267 Further, because the jet multiplicity of $t\bar{t}$ events tends to be higher than WZ, the number of jets
268 in each event is required to be greater than 1. As b-jets are almost invariably produced from top
269 decays, at least one b-tagged jet passing the 70% DL1r WP in each event is required. Various
270 kinematic plots of this region are shown in figure 16.

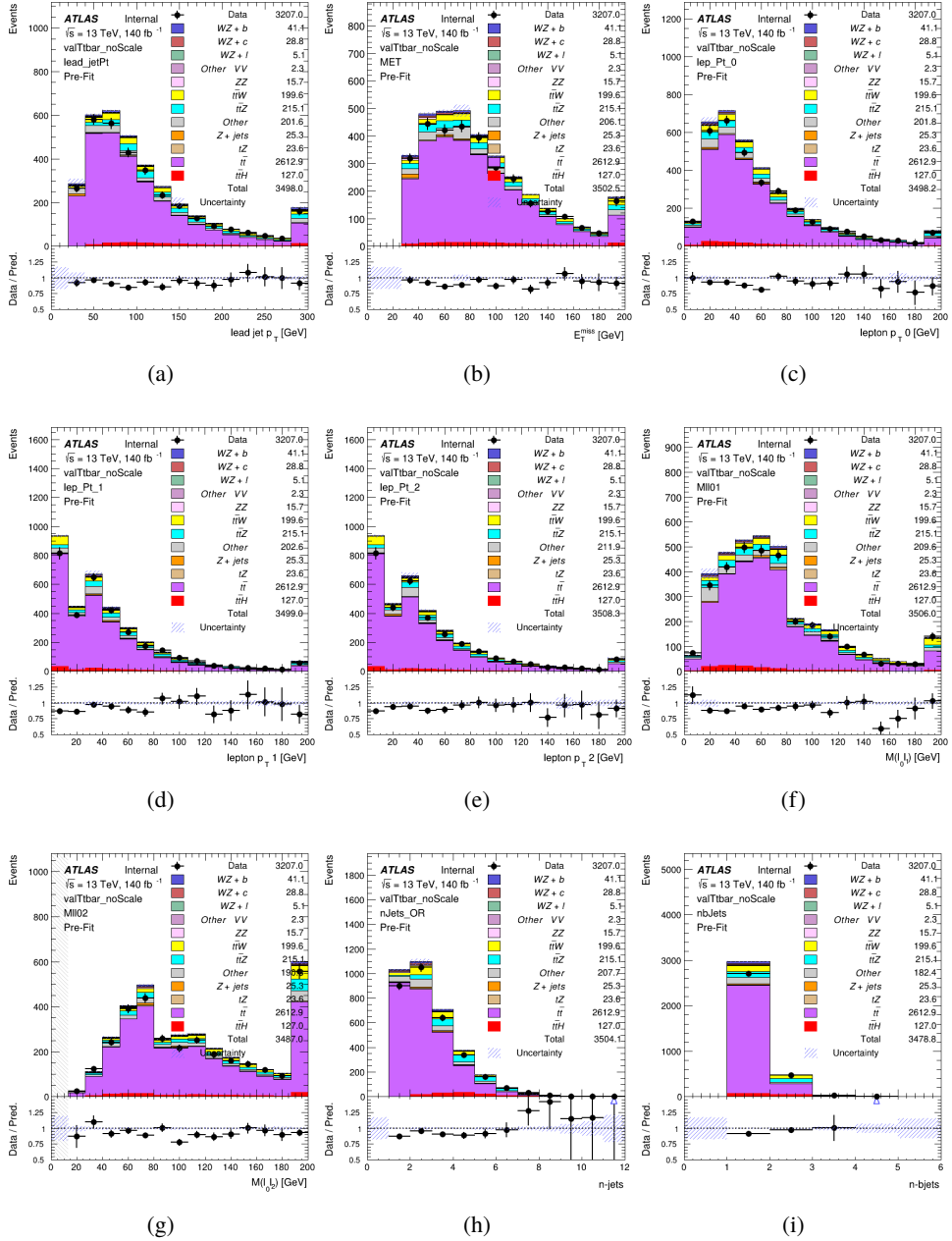


Figure 15: Comparisons between the data and MC distributions in the $t\bar{t}$ validation region for (a) the p_T of the leading jet, (b) the missing transverse energy, (c) the p_T of lepton 0, (d) p_T of lepton 1, (e) p_T of lepton 2, (f) the invariant mass of leptons 0 and 1, (g) the invariant mass of leptons 0 and 2, (h) the number of jets, (i) the number of b-tagged jets.

271 The shape of each distribution agrees quite well between data and MC, with a constant offset
 272 between the two. This is accounted for by applying a constant correction factor of 0.883 to the $t\bar{t}$

273 MC prediction. Plots showing the kinematics of the $t\bar{t}$ VR after this correction factor has been
 274 applied are shown in figure ??.

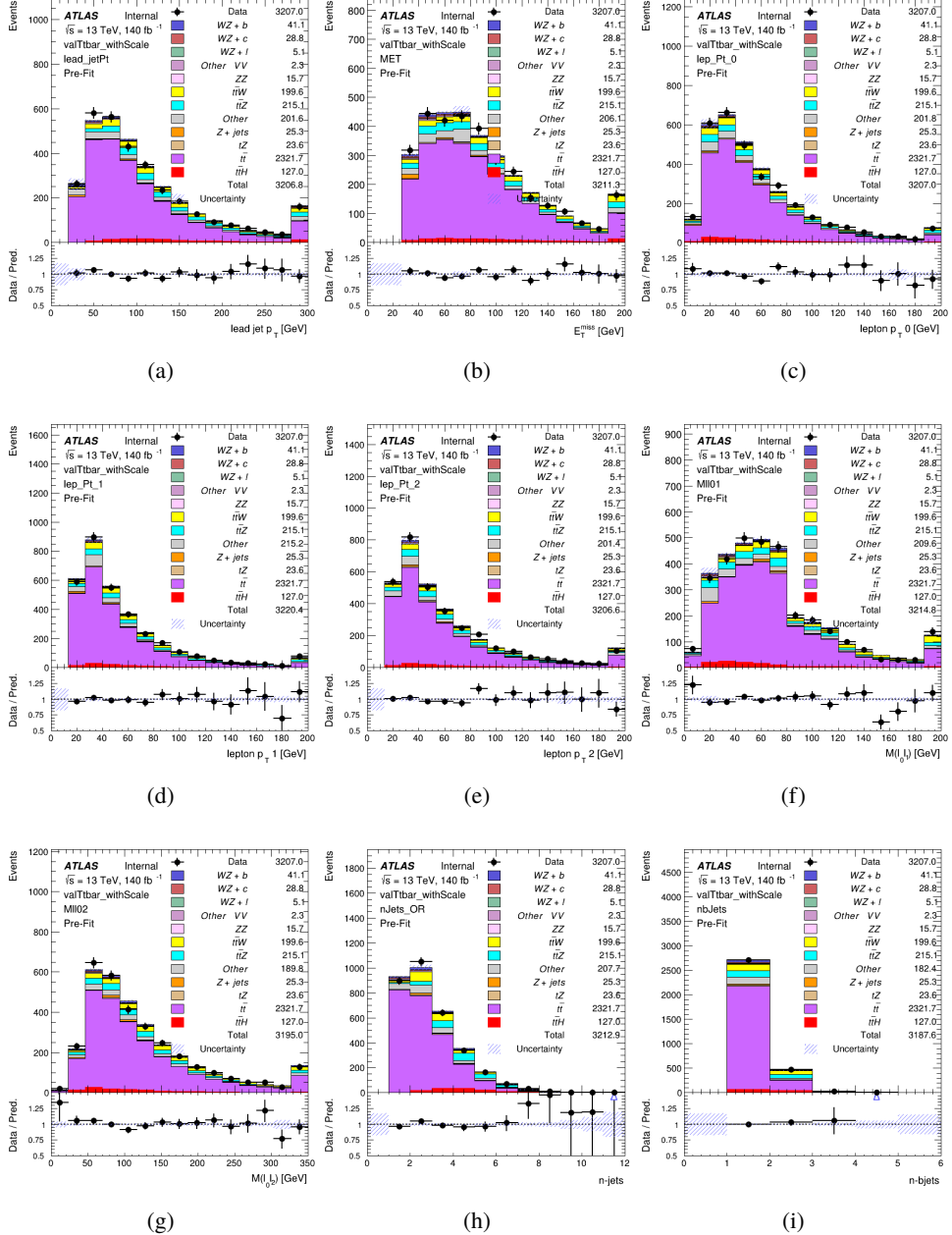


Figure 16: Comparisons between the data and MC distributions in the $t\bar{t}$ validation region after the correction factor has been applied for (a) the p_T of the leading jet, (b) the missing transverse energy, (c) the p_T of lepton 0, (d) p_T of lepton 1, (e) p_T of lepton 2, (f) the invariant mass of leptons 0 and 1, (g) the invariant mass of leptons 0 and 2, (h) the number of jets, (i) the number of b-tagged jets.

275 The modeling is further validated by looking at the yield in the $t\bar{t}$ VR for each DL1r WP, giving
 276 a clearer correspondence to the signal regions used in the fit. Each region shown in figure 20
 277 requires one or more jets pass the listed WP, with no jets passing the next highest WP.

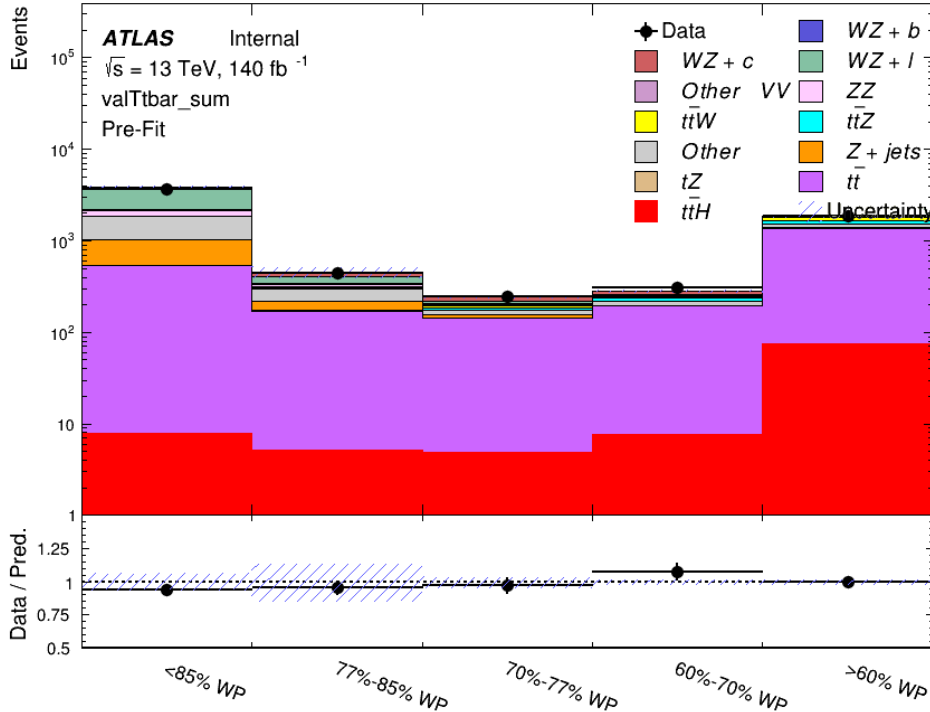


Figure 17: Data and MC comparisons for each DL1r WP for both 1-jet and 2-jet regions, after the $t\bar{t}$ VR selection and correction factor have been applied

278 As data and MC are found to agree within 10% for each of these working points, a 10% systematic
 279 uncertainty on the $t\bar{t}$ prediction is included for the analysis.

280 5.3.2 Z+jets Validation

281 Similar to $t\bar{t}$, a non-prompt Z+jets validation region is produced in order to validate the MC
 282 predictions. The lepton requirements remain the same as the preselection region. Because no
 283 neutrinos are present for this process, the E_T^{miss} cut is reversed, requiring $E_T^{\text{miss}} < 30 \text{ GeV}$. This
 284 also ensures this validation region is orthogonal to the preselection region. Further, the number
 285 of jets in each event is required to be greater than or equal to one. Various kinematic plots of this
 286 region are shown below. The general agreement between data and MC in each of these suggests
 287 that the non-prompt contribution of Z+jets is well modeled by Monte Carlo.

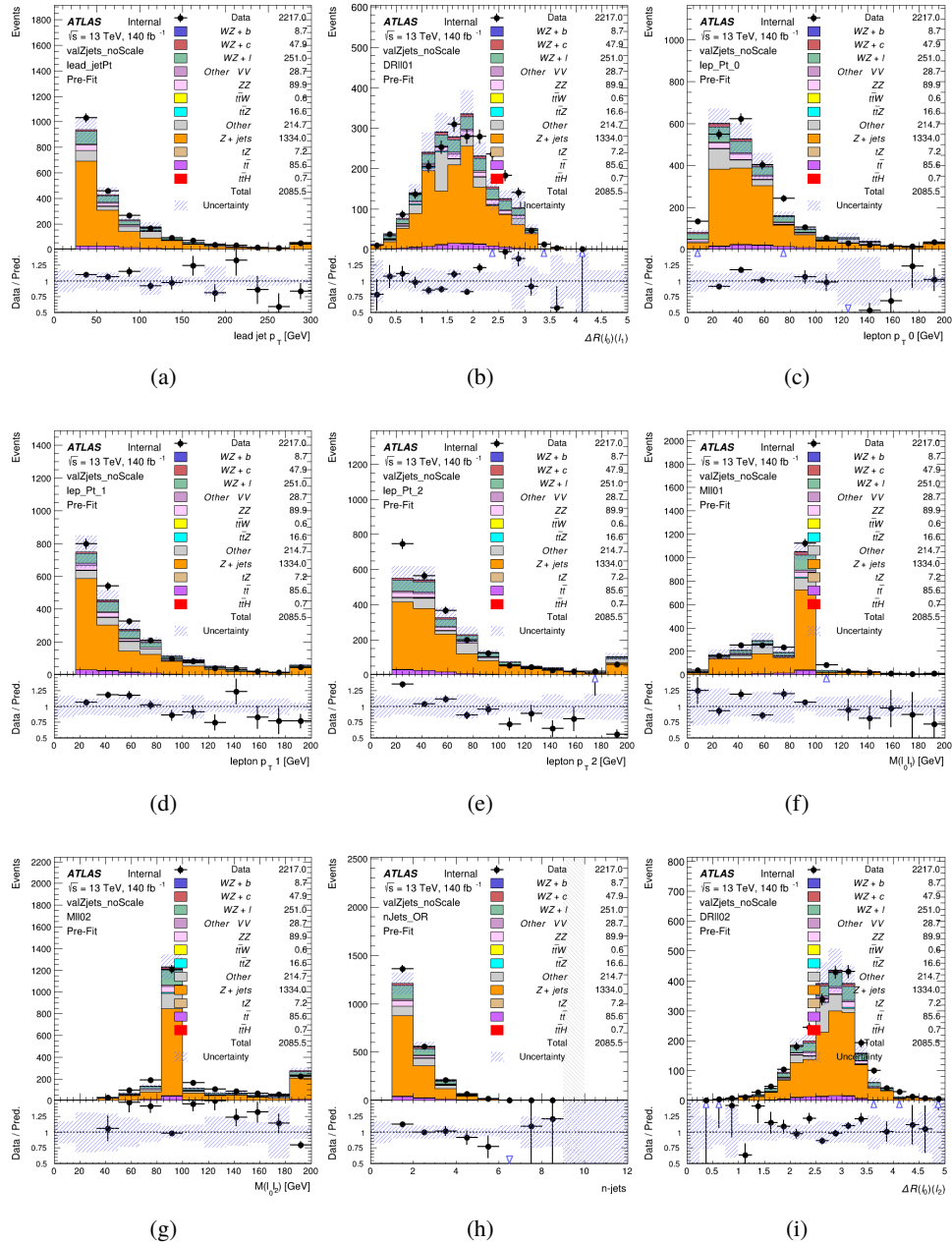


Figure 18: Comparisons between the data and MC distributions in the $Z+jets$ validation region for (a) the p_T of the leading jet, (b) ΔR between leptons 0 and 1, (c) the p_T of lepton 0, (d) p_T of lepton 1, (e) p_T of lepton 2, (f) the invariant mass of leptons 0 and 1, (g) the invariant mass of leptons 0 and 2, (h) the number of jets, (i) ΔR between leptons 0 and 2. Includes only statistical uncertainties

288 While there is general agreement between data and MC within statistical uncertainty, the shape

289 of the p_T spectrum of lepton 2 is found to differ. To account for this discrepancy, a variable
290 correction factor is applied to Z+jets. χ^2 minimization of the lepton 2 p_T spectrum is performed
291 to derive a correction factor of $1.53 - 6.6 * 10^{-6}(\text{lep_Pt_2})$. Kinematic plots of the Z + jets
292 validation region after this correction factor has been applied are shown in figure ??.

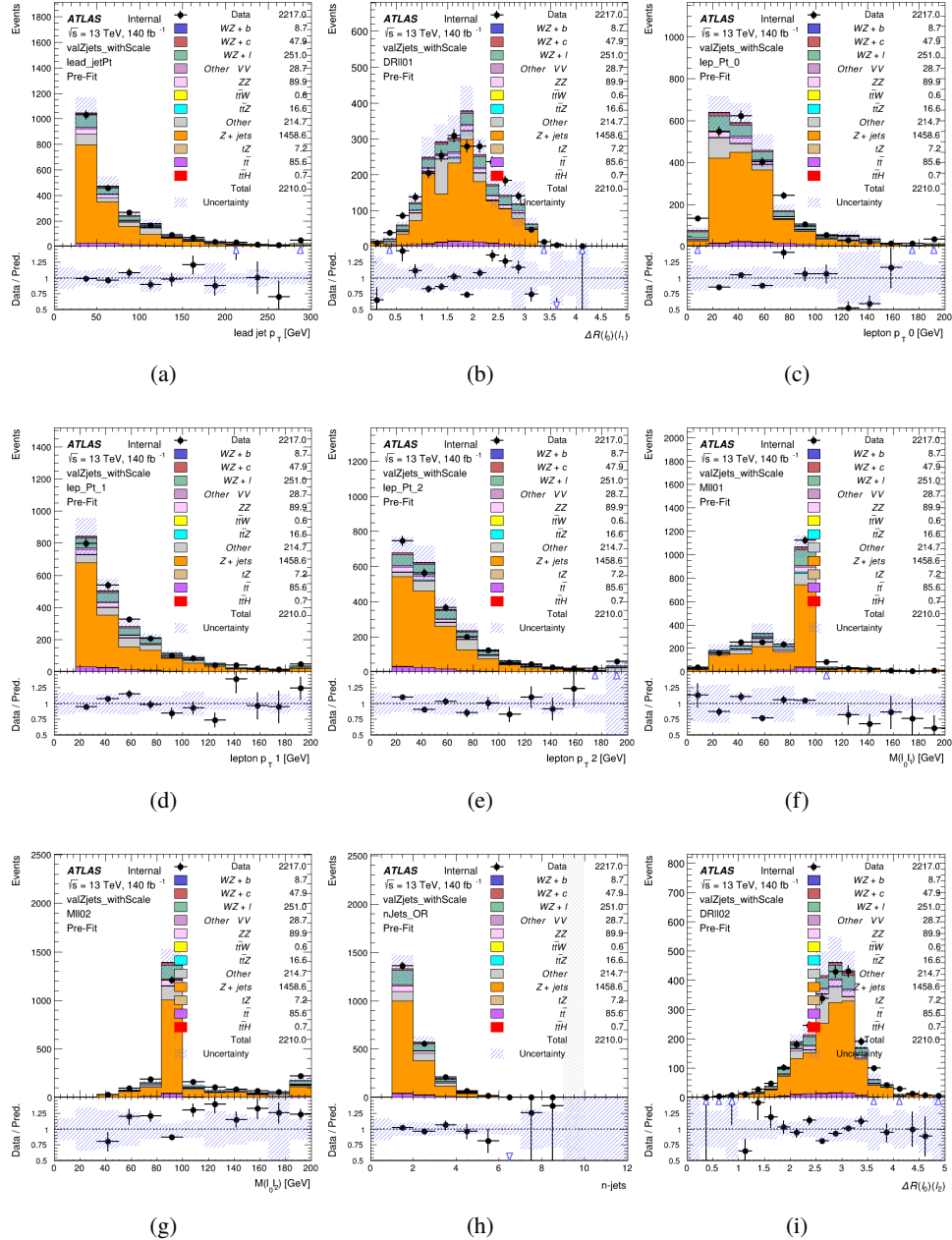


Figure 19: Comparisons between the data and MC distributions in the Z+jets validation region after the correction factor has been applied for (a) the p_T of the leading jet, (b) ΔR between leptons 0 and 1, (c) the p_T of lepton 0, (d) p_T of lepton 1, (e) p_T of lepton 2, (f) the invariant mass of leptons 0 and 1, (g) the invariant mass of leptons 0 and 2, (h) the number of jets, (i) ΔR between leptons 0 and 2

293 The modeling is further validated by looking at the yield in the Z+jets VR for each DL1r WP,

294 giving a clearer correspondence to the signal regions used in the fit. Each region shown in figure
 295 20 requires one or more jets pass the listed WP, with no jets passing the next highest WP.

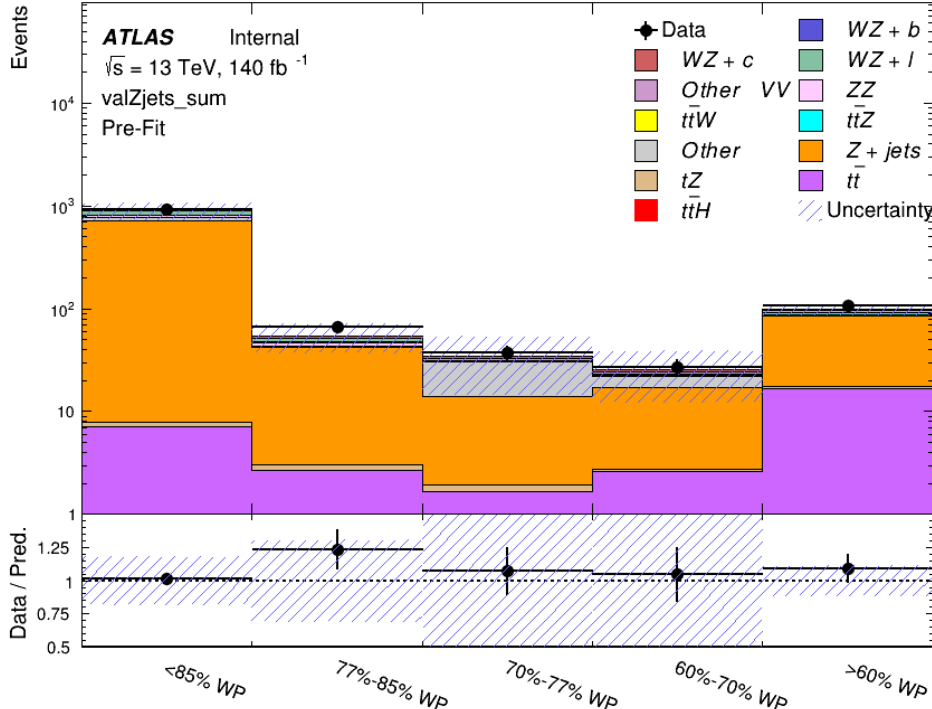


Figure 20: Data and MC comparisons for each DL1r WP for both 1-jet and 2-jet regions, after the Z+jets VR selection and correction factor have been applied

296 For each of the working points considered, the data falls within 20% of the MC prediction once
 297 this correction factor has been applied. Therefore, a 20% systematic uncertainty is applied to Z
 298 + jets in the analysis.

299 6 tZ Interference Studies and Separation Multivariate Analysis

300 Because it includes an on-shell Z boson as well as a b-jet and W from the top decay, tZ
 301 production represents an identical final state to WZ + b-jet. This implies the possibility of matrix
 302 level interference between these two processes not accounted for in the Monte Carlo simulations,
 303 which consider the two processes independently. Truth level studies are performed in order to
 304 estimate the impact of these interference effects.

305 Because tZ produces a final state identical to signal, it represents a predominant background in
 306 the most signal enriched regions. That is, the region with one jet passing the 60% DL1r WP.

307 Therefore, a boosted decision tree (BDT) algorithm is trained using TMVA [10] to separate WZ
308 + heavy flavor from tZ.

309 Separation between tZ and WZ + heavy flavor is achieved in part by reconstructing the invariant
310 mass of the top candidate, which clusters more closely to the top mass for tZ than WZ + heavy
311 flavor.

312 The result of this BDT is used to create a tZ enriched region in the fit, reducing its impact on the
313 measurement of WZ + heavy flavor.

314 **6.1 Interference Studies**

315 In order to estimate the matrix level interference effects between tZ and WZ + b-jet, two different
316 sets of simulations are produced using MadGraph 5 [Madgraph] - one which simulates these
317 two processes independently, and another where they are produced simultaneously, such that
318 interference effects are present. These two sets of samples are then compared, and the difference
319 between them can be taken to represent any interference effects.

320 MadGraph simulations of 10,000 tZ and 10,000 WZ + b-jet events are produced, along with
321 20,000 events where both are present, in the fiducial region where three leptons and at least one
322 jet are produced.

323 The kinematics of these samples are shown below:

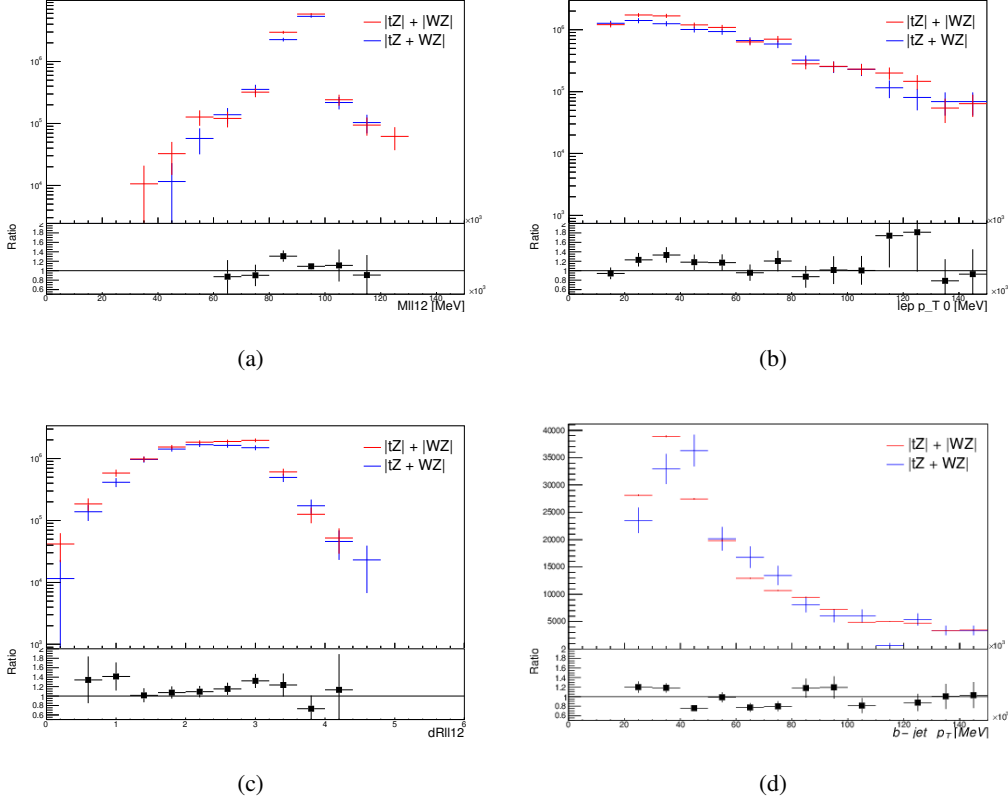


Figure 21: Comparisons between (a) the invariant mass of the Z-candidate, (b) the p_T of the leading lepton, (c) $\Delta(R)$ of the two leptons that form the Z-candidate, and (d) the p_T of the b-jet, for WZ and tZ events generated with interference effects (blue) and without interference effects (red).

324 6.2 Top Mass Reconstruction

325 The reconstruction of the top mass follows the procedure described in detail in section 6.1 of
 326 [11]. The mass of the top quark candidate is reconstructed from the jet, the lepton not included
 327 in the Z-candidate, and a reconstructed neutrino. In the case that there is one jet in the event,
 328 there is only possible b-jet candidate. For events with two jets, the jet with the highest DL1r
 329 score is used.

330 The neutrino from the W decay is expected to be the only source of E_T^{miss} . Therefore, the E_T^{miss}
 331 and ϕ of the neutrino are taken from the E_T^{miss} measurement. This leaves the z-component of
 332 the neutrino momentum, p_{VZ} as the only unknown.

333 This unknown is solved for by taking the combined invariant mass of the lepton and neutrino to
 334 give the invariant mass of the W boson:

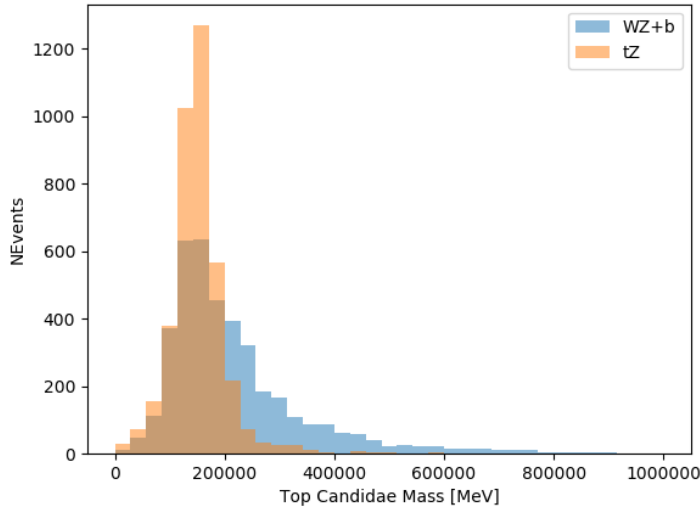


Figure 22: Reconstructed top mass distributions for tZ and WZ + b, measured in MeV.

$$(p_l + p_\nu)^2 = m_W^2$$

Expanding this out into components, this equation gives:

$$\sqrt{p_{T\nu}^2 + p_{z\nu}^2} E_l = \frac{m_W^2 - m_l^2}{2} + p_{T\nu}(p_{lx}\cos\phi_\nu + p_{ly}\sin\phi_\nu) + p_{lz}p_{\nu z}$$

This equation gives two solutions for $p_{\nu z}$. For cases where only one of these solutions is real, that is taken as the value of $p_{\nu z}$. For instances with two real solutions, the one which is shown to be correct in the largest fraction of simulations is taken. For cases when no real solution is found, often because of detector effects, the value of E_T^{miss} is varied in decreasing increments of 100 MeV until a real solution is found.

The reconstructed top mass distribution for tZ and WZ + b can be seen in figure 22.

6.3 tZ BDT

A Boosted Decision Tree (BDT), specifically XGBoost [xgboost_cite], is used to provide separation between tZ and WZ+b. The following kinematic variables are used as inputs:

- The invariant mass of the reconstructed top candidate
- p_T of each of the leptons, jet
- The invariant mass of each combination of lepton pairs, $M(l\bar{l})$

- 350 • E_T^{miss}
 351 • Distance between each combination of leptons, $\Delta R(l_1 l_2)$
 352 • Distance between each lepton and the jet, $\Delta R(l_j)$

353 The training samples included only events meeting the requirements of the 1-jet, >60% region,
 354 i.e. passing all the selection described in section 5 and having exactly one jet which passes the
 355 tightest (60%) DL1r working point.

356 The distributions of a few of these features for both signal and background is shown in figure
 357 23.

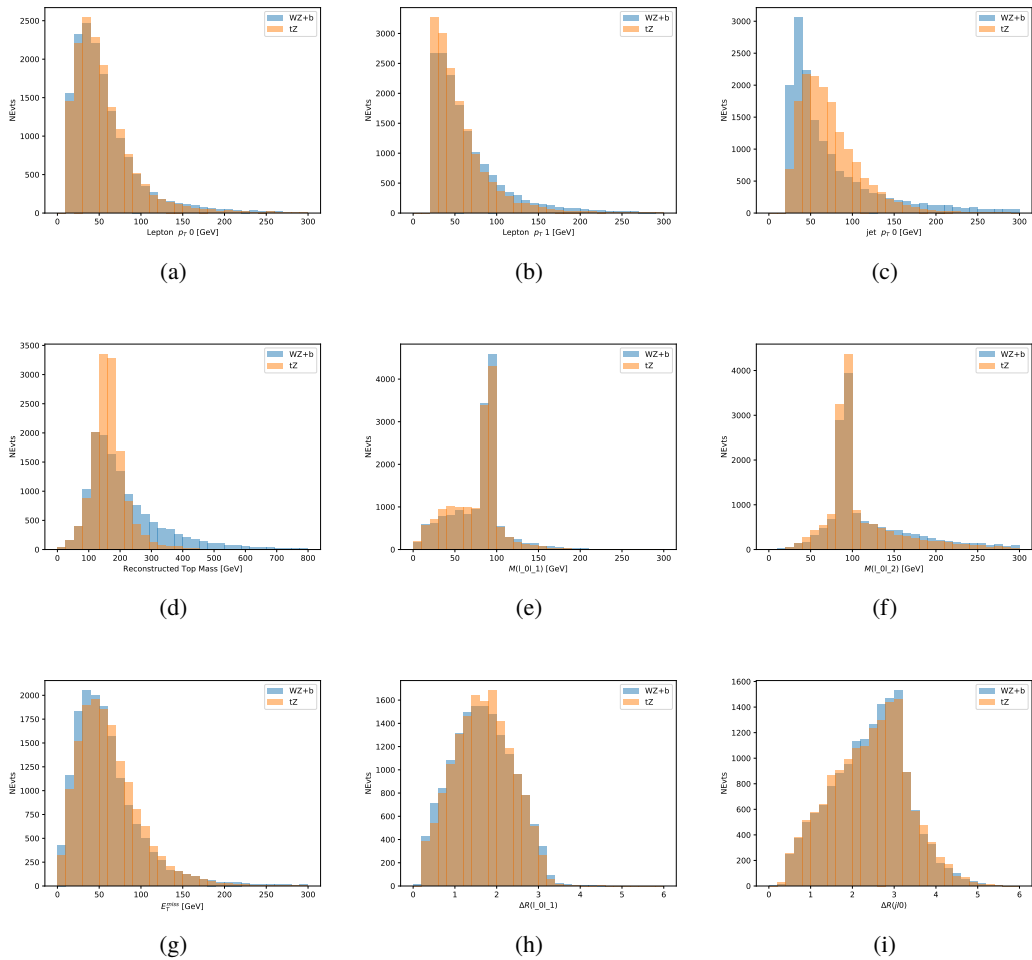


Figure 23: Distribution of input features of the BDT for signal (WZ) and background (tZ). Both are scaled to an equal number of events. (a), (b) and (c) show the p_T of lepton 0, lepton 1, and the jet, (d) show the reconstructed top mass, (e) and (f) show the invariant mass of leptons 0 and 1, leptons 0 and 2. (g) shows the E_T^{miss} of each event. (h) and (i) show the ΔR between lepton 0 and lepton 1, and the jet.

358 A sample of 20,000 background (tZ) and signal ($WZ+b$) Monte Carlo events are used to train
 359 the BDT. And additional 5,000 events are reserved for testing the model, in order to prevent
 360 over-fitting. A total of 750 decision trees with a maximum depth of 6 branches are used to build
 361 the model. These parameters are chosen empirically, by training several models with different
 362 parameters and selecting the one that gave the best separation for the test sample.

363 The results of the BDT training are shown in figure 24. The output scores for both signal and
 364 background events is shown on the left. The right shows the receiving operating characteristic
 365 (ROC) curve that results from the MVA. The ROC curve represents the background rejection
 366 as a function of signal efficiency, where each point on the curve represents a different response
 367 score. The ROC curve of the BDT is compared to the performance of using an optimal set of flat
 368 selections on the same set of input variables.

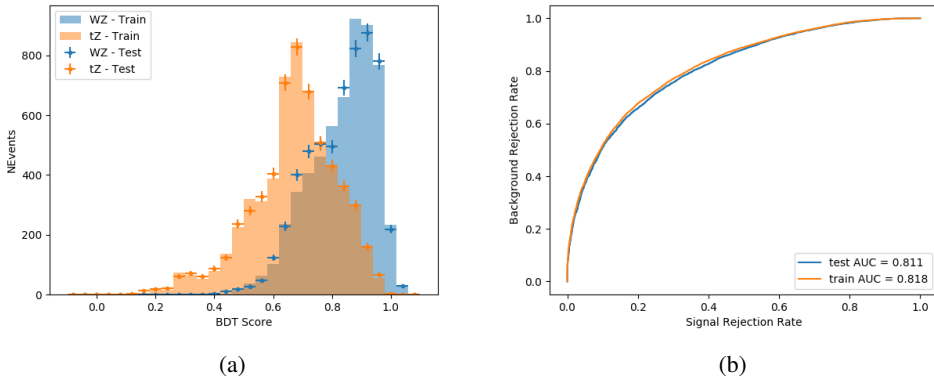


Figure 24: Distribution of the BDT response for signal and background events on the left, the ROC curve for the BDT on the right.

369 The relative important of each input feature in the model, measured by how often they appeared
 370 in the decision trees, is shown in figure 25.

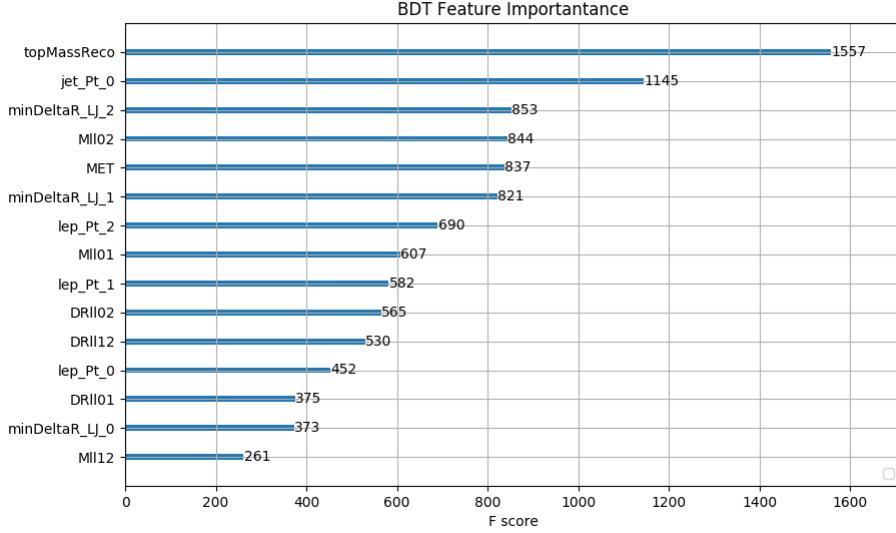


Figure 25: Relative importance of each input feature in the model.

371 These results suggest that some amount of separation can be achieved between these two pro-
 372 cesses, with a high BDT score selecting a set of events that is pure in $WZ + b$.

373 7 Systematic Uncertainties

374 The systematic uncertainties that are considered are summarized in table 9. These are imple-
 375 mented in the fit either as a normalization factors or as a shape variation or both in the signal
 376 and background estimations. The numerical impact of each of these uncertainties is outlined in
 377 section 8.

378 The uncertainty in the combined integrated luminosity is derived from a calibration of the
 379 luminosity scale performed for 13 TeV proton-proton collisions [12], [LUCID2]..

380 The experimental uncertainties are related to the reconstruction and identification of light leptons
 381 and b-tagging of jets, and to the reconstruction of E_T^{miss} . The sources which contribute to the
 382 uncertainty in the jet energy scale [13] are decomposed into uncorrelated components and treated
 383 as independent sources in the analysis.

384 The uncertainties in the b-tagging efficiencies measured in dedicated calibration analyses [14] are
 385 also decomposed into uncorrelated components. The large number of components for b-tagging
 386 is due to the calibration of the distribution of the MVA discriminant.

387 The systematic uncertainties associated with the signal and background processes are accounted
 388 for by varying the cross-section of each process within its uncertainty.

Table 9: Sources of systematic uncertainty considered in the analysis.

Systematic uncertainty	Components
Luminosity	1
Pileup reweighting	1
Physics Objects	
Electron	6
Muon	15
Jet energy scale and resolution	28
Jet vertex fraction	1
Jet flavor tagging	131
E_T^{miss}	3
Total (Experimental)	186
Background Modeling	
Cross section	24
Renormalization and factorization scales	10
Parton shower and hadronization model	2
Shower tune	4
Total (Signal and background modeling)	40
Total (Overall)	226

³⁸⁹ The full list of systematic uncertainties considered in the analysis is summarized in tables 10, 11
³⁹⁰ and 12.

³⁹¹

Experimental Systematics on Leptons and E_T^{miss}			
Type	Description	Systematics Name	Application
Trigger			
Scale Factors	Trigger Efficiency	lepSFTrigTight_MU(EL)_SF_Trigger_STAT(SYST)	Event Weight
Muons			
Efficiencies	Reconstruction and Identification	lepSFObjTight_MU_SF_ID_STAT(SYST)	Event Weight
	Isolation	lepSFObjTight_MU_SF_Isol_STAT(SYST)	Event Weight
	Track To Vertex Association	lepSFObjTight_MU_SF_TTVA_STAT(SYST)	Event Weight
p_T Scale	p_T Scale	MUONS_SCALE	p_T Correction
Resolution	Inner Detector Energy Resolution	MUONS_ID	p_T Correction
	Muon Spectrometer Energy Resolution	MUONS_MS	p_T Correction
Electrons			
Efficiencies	Reconstruction	lepSFObjTight_EL_SF_ID	Event Weight
	Identification	lepSFObjTight_EL_SF_Reco	Event Weight
	Isolation	lepSFObjTight_EL_SF_Isol	Event Weight
Scale Factor	Energy Scale	EG_SCALE_ALL	Energy Correction
Resolution	Energy Resolution	EG_RESOLUTION_ALL	Energy Correction
E_T^{miss}			
Soft Tracks Terms	Resolution	MET_SoftTrk_ResoPerp	p_T Correction
	Resolution	MET_SoftTrk_ResoPara	p_T Correction
	Scale	MET_SoftTrk_ScaleUp	p_T Correction
	Scale	MET_SoftTrk_ScaleDown	p_T Correction

Table 10: Summary of experimental systematics considered for leptons and E_T^{miss} . Includes type, description, name of systematic as used in the fit, and mode of application. The mode of application indicates the systematic evaluation, e.g. as an overall event re-weighting (Event Weight) or rescaling (p_T Correction).

Experimental Systematics on Jets			
Type	Origin	Systematics Name	Application
Jet Vertex Tagger		JVT	Event Weight
Energy Scale	Calibration Method	JET_21NP_ JET_EffectiveNP_1-19	p_T Correction p_T Correction
	η inter-calibration	JET_EtaIntercalibration_Modelling JET_EtaIntercalibration_NonClosure JET_EtaIntercalibration_TotalStat	p_T Correction p_T Correction p_T Correction
	High p_T jets	JET_SingleParticle_HighPt	p_T Correction
21st January 2021 – PileUp		JET_Pileup_OffsetNPV JET_Pileup_OffsetMu JET_Pileup_PtTerm JET_Pileup_RhoTopology	p_T Correction p_T Correction p_T Correction p_T Correction
	Non Closure	JET_PunchThrough_MC15	p_T Correction
	Flavour	JET_Flavor_Response JET_BJES_Response JET_Flavor_Composition	p_T Correction p_T Correction p_T Correction

Experimental Systematics on b-tagging		
Type	Origin	Systematic Name
Scale Factors	DL1r b-tagger efficiency on b originated jets in bins of η	DL1r_Continuous_EventWeight_B0-29
	DL1r b-tagger efficiency on c originated jets in bins of η	DL1r_Continuous_EventWeight_C0-19
	DL1r b-tagger efficiency on light flavoured originated jets in bins of η and p_T	DL1r_Continuous_EventWeight_Light0-79
	DL1r b-tagger extrapolation efficiency	DL1r_Continuous_EventWeight_extrapolation DL1r_Continuous_EventWeight_extrapolation_from_charm

Table 12: Summary of experimental systematics to be included for b-tagging of jets in the analysis, using the continuous DL1r tagging algorithm. All of the b-tagging related systematics are applied as event weights. From left: type, description, and the name of systematic used in the fit.

³⁹² The cross-section uncertainties applied to background estimates are summarized in table 13.

Process	X-section [%]
tZ	+36 -31
t̄t H (aMC@NLO+Pythia8)	QCD Scale: +5.8 -9.2 PDF(+ α_S): ± 3.6
t̄t Z (aMC@NLO+Pythia8)	QCD Scale: +9.6 -11.3 PDF(+ α_S): ± 4
t̄t W (aMC@NLO+Pythia8)	QCD Scale: +12.9 -11.5 PDF(+ α_S): ± 3.4
VV + b/charm (Sherpa 2.2.1)	± 50
VV + light (Sherpa 2.2.1)	± 6
t̄t	± 20 placeholder
Z + jets	± 25 placeholder
Others	± 50

Table 13: Summary of theoretical uncertainties for MC prediction of backgrounds in the analysis.

³⁹³ 8 Results

³⁹⁴ A separate maximum-likelihood fit is performed over the 1-jet and 2-jet fit regions in order to
³⁹⁵ extract the best-fit value of the WZ + b-jet and WZ + charm jet contributions. The WZ + b,

396 WZ + charm and WZ + light contributions are allowed to float, with the remaining background
 397 contributions are held fixed. **The current fit strategy treats the WZ + b-jet contribution as**
 398 **the parameter of interest, with the normalization of the WZ + charm and the WZ + light**
 399 **contributions taken as systematic uncertainties. This could however be adjusted, depending**
 400 **on whether it is decided the goal of the analysis should be to measure WZ+b specifically or**
 401 **WZ + heavy flavor overall.** The result of the fit is used to extract the cross-section of WZ +
 402 heavy-flavor production.

403 A maximum likelihood fit to data is performed simultaneously in the regions described in section
 404 5. The parameters μ_{WZ+b} , $\mu_{WZ+charm}$, $\mu_{WZ+light}$, where $\mu = \sigma_{\text{observed}}/\sigma_{\text{SM}}$, are extracted
 405 from the fit.

406 8.1 1-jet Fit Results

407 **The results of the fit are currently blinded.** The post-fit yields in each region are summarized
 408 in figure 26.

409 A post-fit summary plot of the 1-jet fitted regions is shown in figure 27:

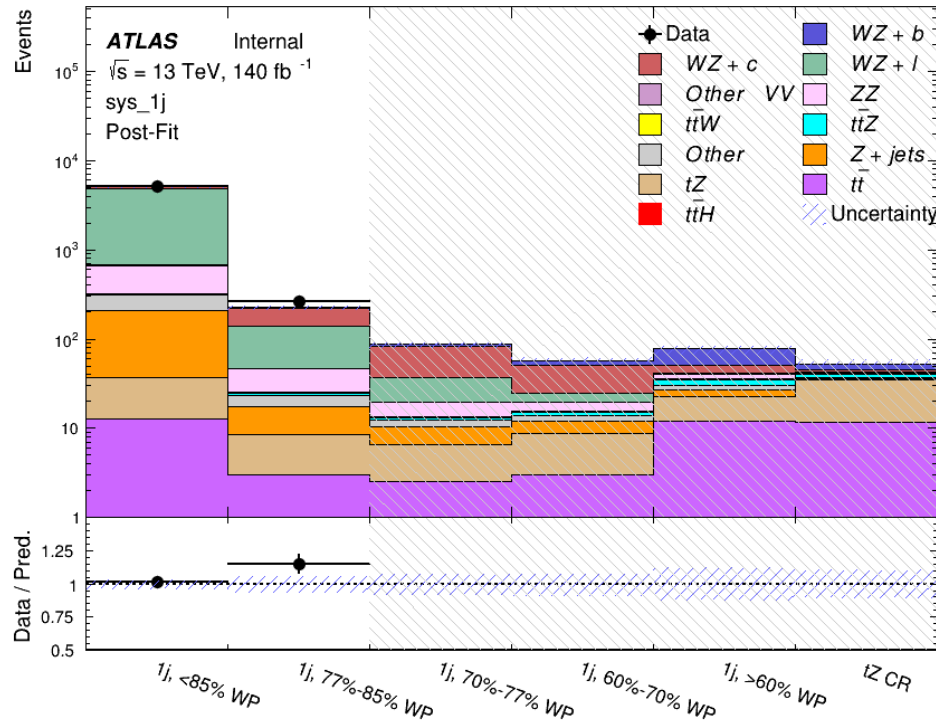


Figure 27: Post-fit summary of the 1-jet fit regions.

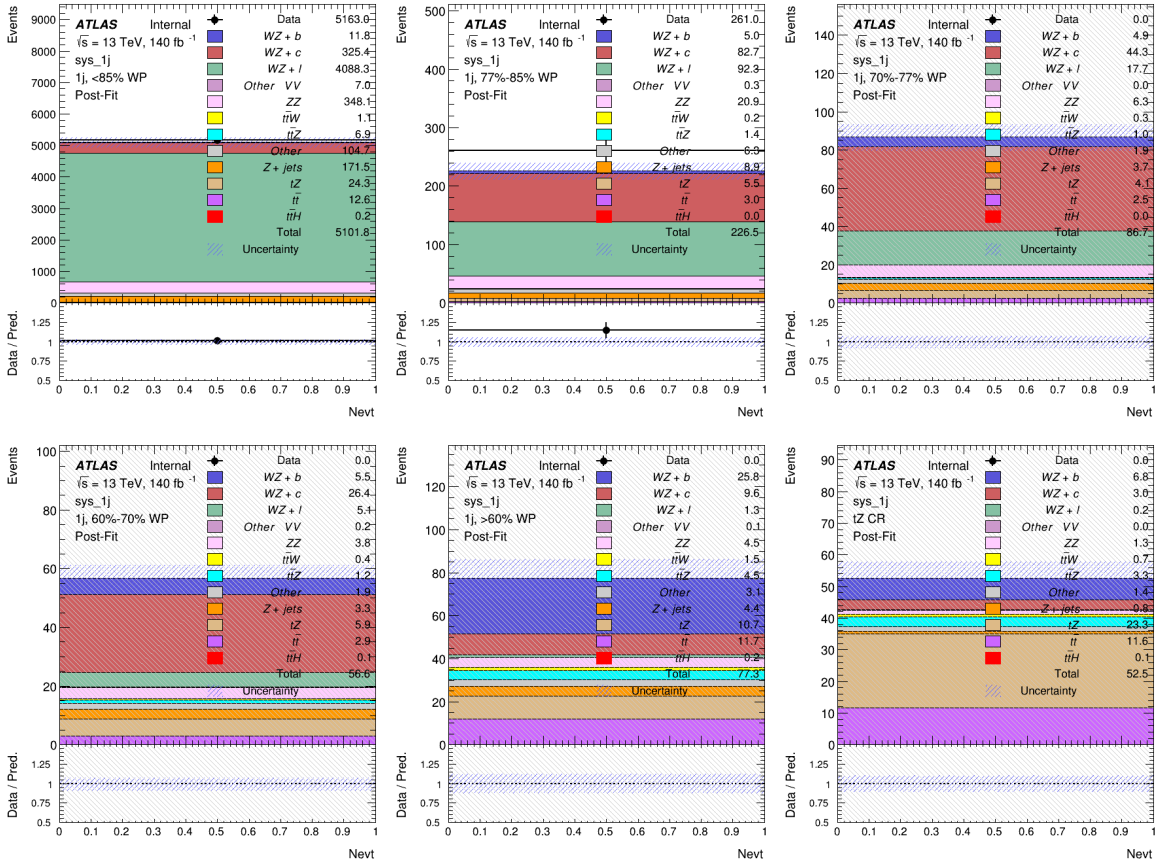


Figure 26: Data/MC results in each of the 1-jet regions after the fit has been performed.

As described in section 7, there are 226 systematic uncertainties that are considered as NPs in the fit. These NPs are constrained by Gaussian or log-normal probability density functions. The latter are used for normalisation factors to ensure that they are always positive. The expected numbers of signal and background events are functions of the likelihood. The prior for each NP is added as a penalty term, decreasing the likelihood as it is shifted away from its nominal value.

The impact of each systematic uncertainty is calculated by performing the fit with the parameter of interest held fixed, varied from its fitted value by its uncertainty, and calculating $\delta\mu$ relative to the baseline fit. The impact of the most significant systematic uncertainties is summarized in table 14.

Uncertainty Source	$\Delta\mu$	
WZ + charm cross-section	-0.1966	0.2171
tZ cross-section	-0.1521	0.1518
WZ + light cross-section	0.1485	-0.1411
Other VV + b cross-section	-0.1115	0.1163
Flavor Tagging	0.0955	0.0957
Jet Energy Scale	0.0613	0.081
t <bar>t</bar>	-0.0662	0.0654
Luminosity	-0.0609	0.0655
Z + jets cross-section	-0.0284	0.0284
Other VV + charm cross-section	0.0207	-0.0202
Muon Trigger Scale Factor	0.019	0.0209
Total Systematic Uncertainty	0.3511	0.3679

Table 14: Summary of the most significant sources of systematic uncertainty on the measurement of WZ + b with exactly one associated jet.

420 The ranking and impact of those nuisance parameters with the largest contribution to the overall
421 uncertainty is shown in figure 28.

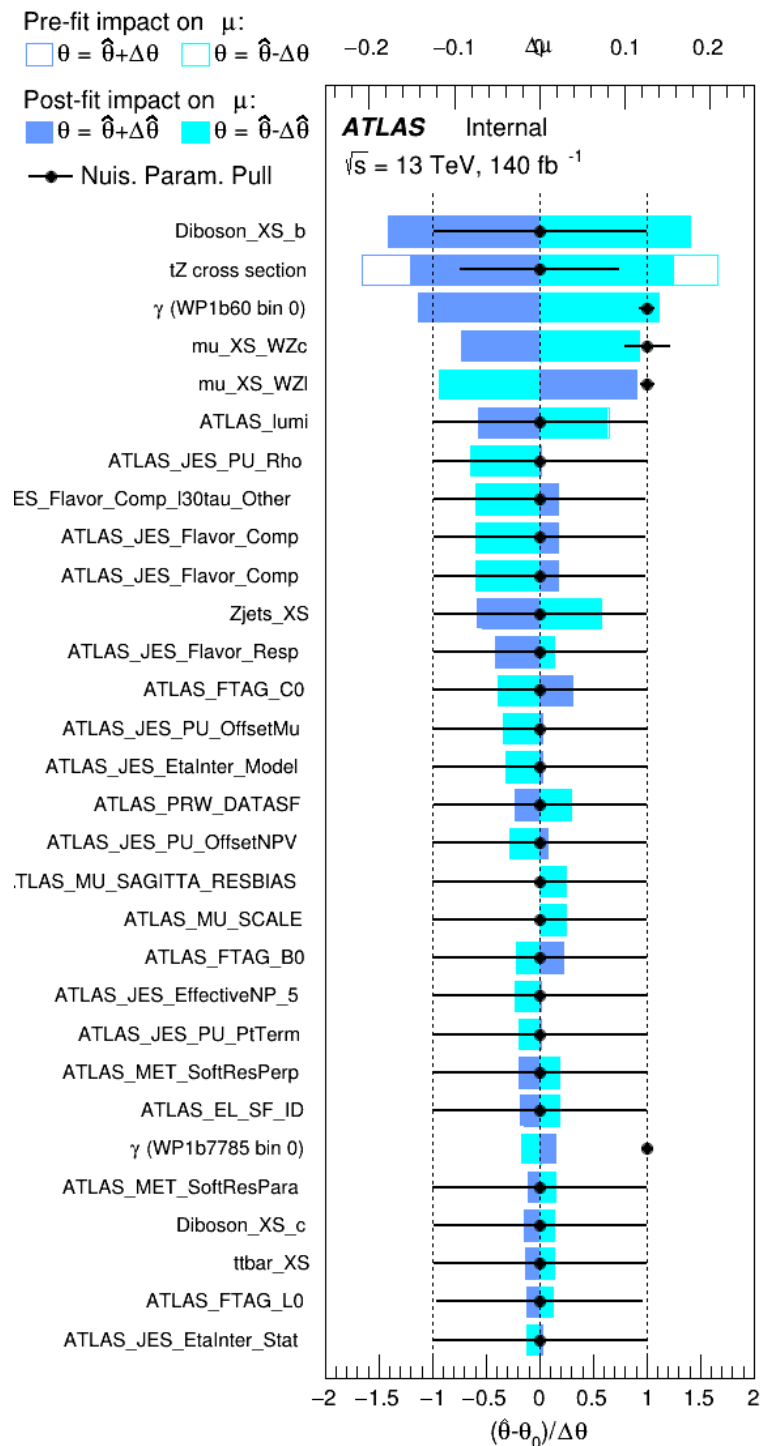


Figure 28: Impact of systematic uncertainties on the signal-strength of $WZ + b$ for events with exactly one jet

422 The large impact of the Jet Energy Scale and Jet Flavor Tagging is unsurprising, as the shape
 423 of the fit regions depends heavily on the modeling of the jets. The other major sources of
 424 uncertainty come from background modelling and cross-section uncertainty. The pie charts in
 425 figure 29 show that for the modelling uncertainties that contribute most correspond to the most
 426 significant backgrounds.

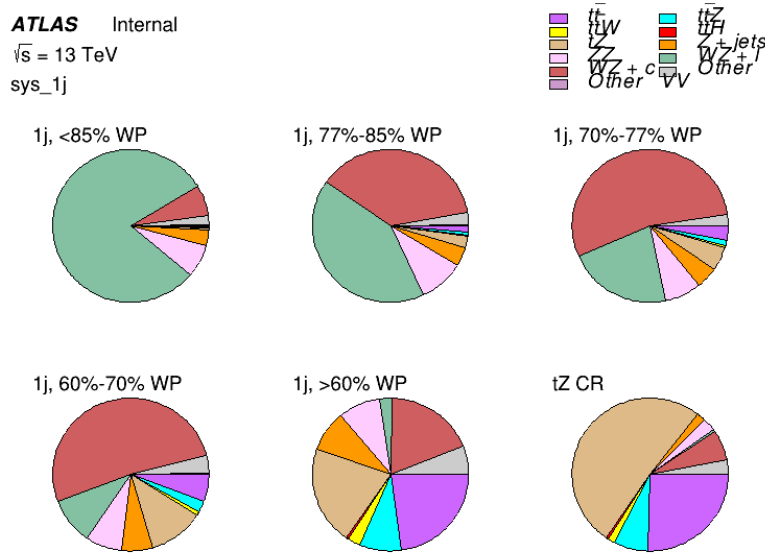


Figure 29: Post-fit background composition of the fit regions.

427 The correlations between these nuisance parameters are summarized in figure 30.

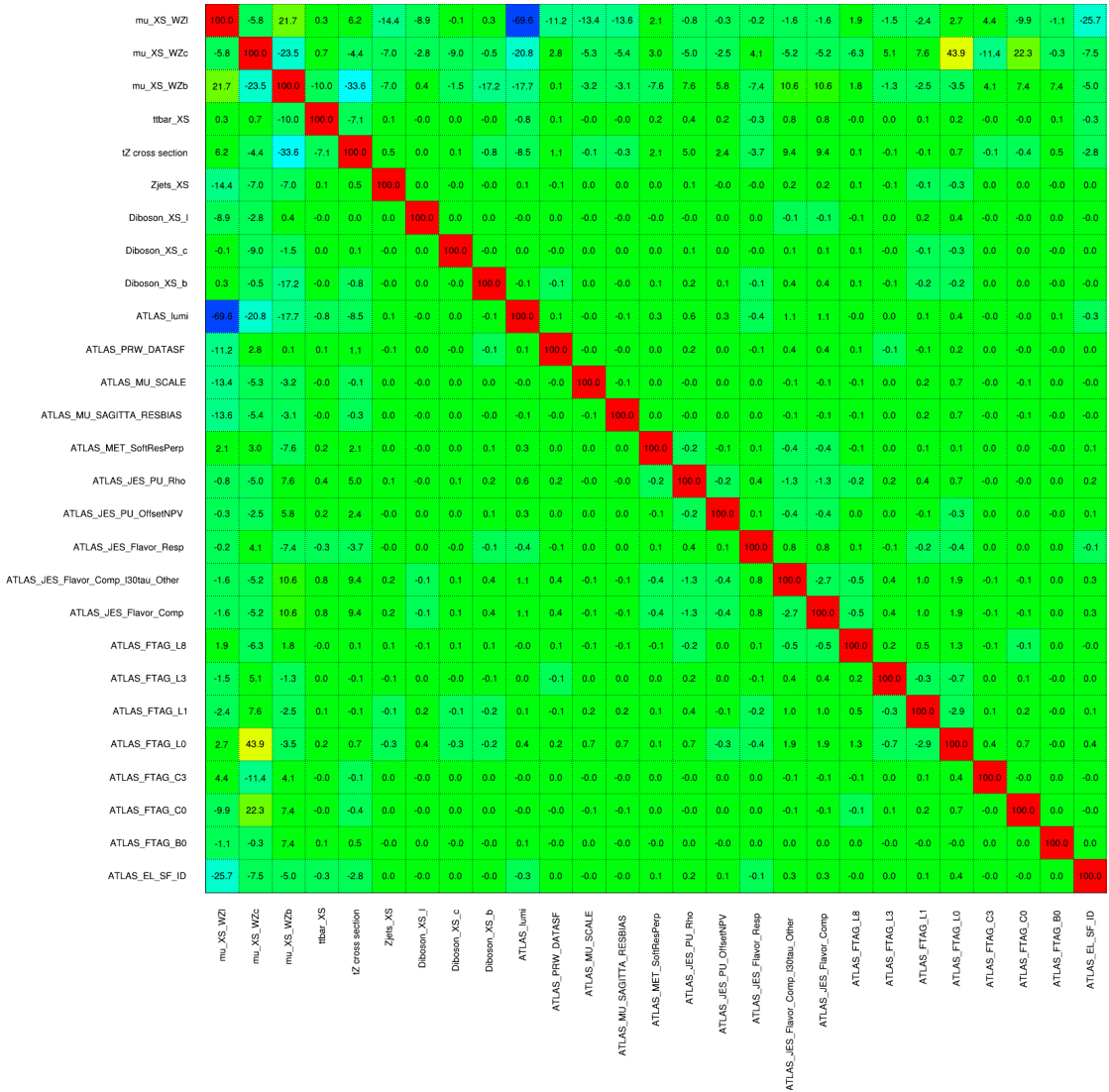


Figure 30: Correlations between nuisance parameters

428 The negative correlations between $\mu_{WZ+charm}$ and μ_{WZ+b} and $\mu_{WZ+light}$ are expected: $WZ +$
429 charm is present in both the $WZ + b$ and $WZ + light$ enriched regions, therefore increasing the
430 fraction of charm requires increasing the fraction of $WZ + b$ and $WZ + light$. This reasoning
431 also explains the positive correlation between μ_{WZ+b} and $\mu_{WZ+light}$.

432 Two of the major backgrounds in the region with the highest purity of $WZ + b$ are tZ and Other
433 $VV + b$, explaining the negative correlations between μ_{WZ+b} and the tZ cross section, and the
434 $VV + b$ cross section.

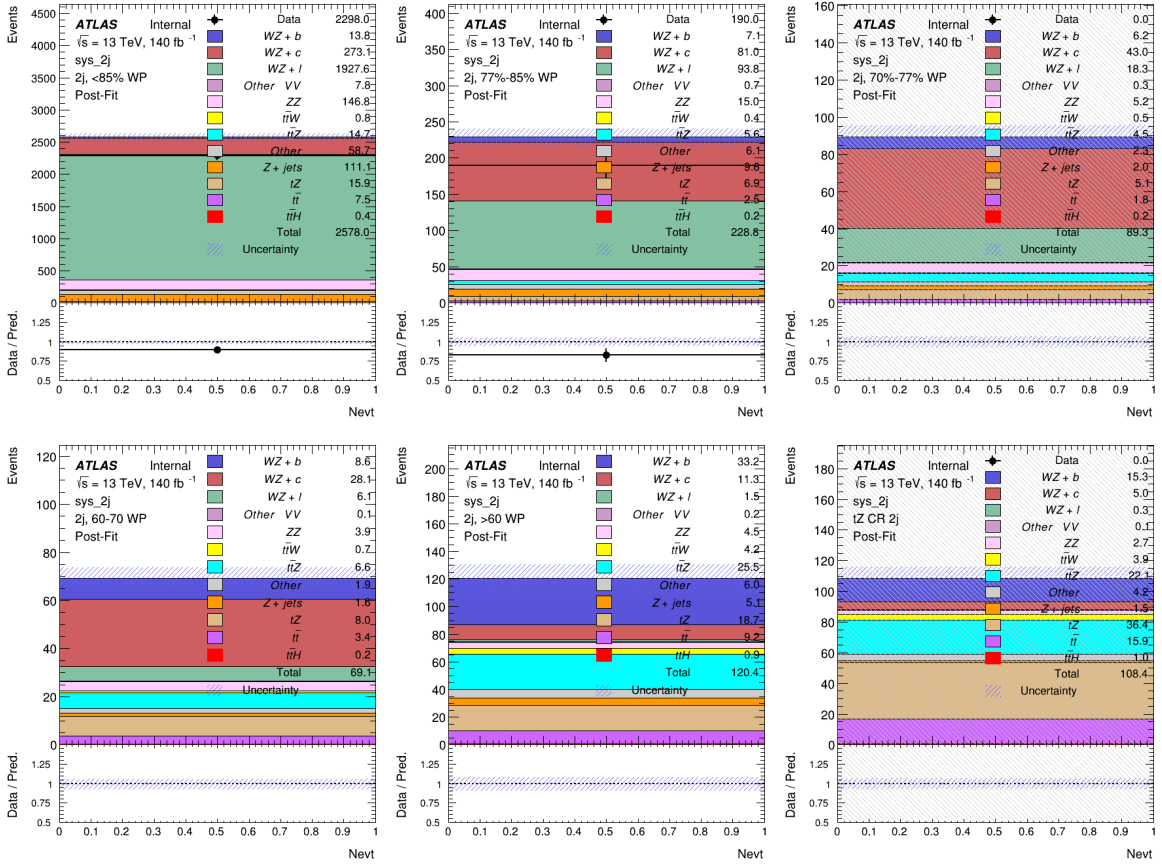


Figure 31: Data/MC results in each of the regions in the 2-jet fit after the fit has been performed.

435 The high correlation between the luminosity and $\mu_{WZ+\text{light}}$ arises from the fact that the uncer-
 436 tainty on $\mu_{WZ+\text{light}}$ is very low (around 4%). Small changes in luminosity cause a change in
 437 the yield of $WZ + \text{light}$ that is large compared to its uncertainty, producing a large correlation
 438 between these two parameters.

439 8.2 2-jet Fit Results

440 **The results of the fit are currently blinded.** The post-fit yields in each region are summarized
 441 in figure 31.

442 A post-fit summary plot of the fitted regions is shown in figure 32:

443 The same set of systematic uncertainties consider for the 1-jet fit are included in the 2-jet fit as
 444 well. The impact of the most significant systematic uncertainties is summarized in table 15.

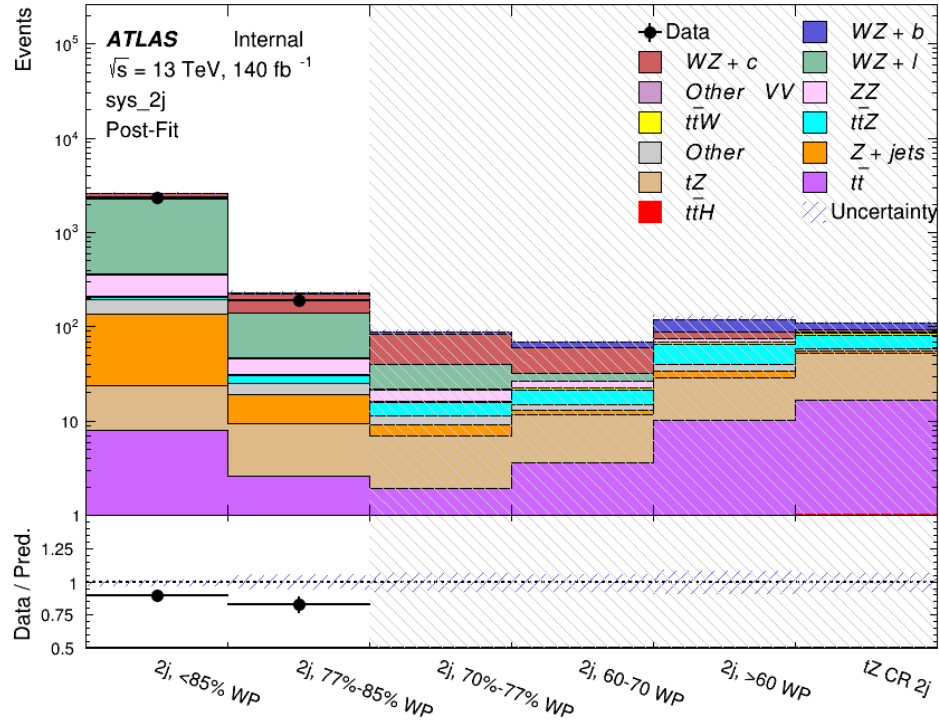


Figure 32: Post-fit summary of the fit over 2-jet regions.

Uncertainty Source	$\Delta\mu$	
WZ + charm cross-section	-0.1966	0.2171
tZ cross-section	-0.1521	0.1518
WZ + light cross-section	0.1485	-0.1411
Other VV + b cross-section	-0.1115	0.1163
Flavor Tagging	0.0955	0.0957
Jet Energy Scale	0.0613	0.081
t̄t cross-section	-0.0662	0.0654
Luminosity	-0.0609	0.0655
Z + jets cross-section	-0.0284	0.0284
Other VV + charm cross-section	0.0207	-0.0202
Muon Trigger Scale Factor	0.019	0.0209
Total Systematic Uncertainty	0.3511	0.3679

Table 15: Summary of the most significant sources of systematic uncertainty on the measurement of WZ + b 2-jet events.

The ranking and impact of those nuisance parameters with the largest contribution to the overall uncertainty is shown in figure 33.

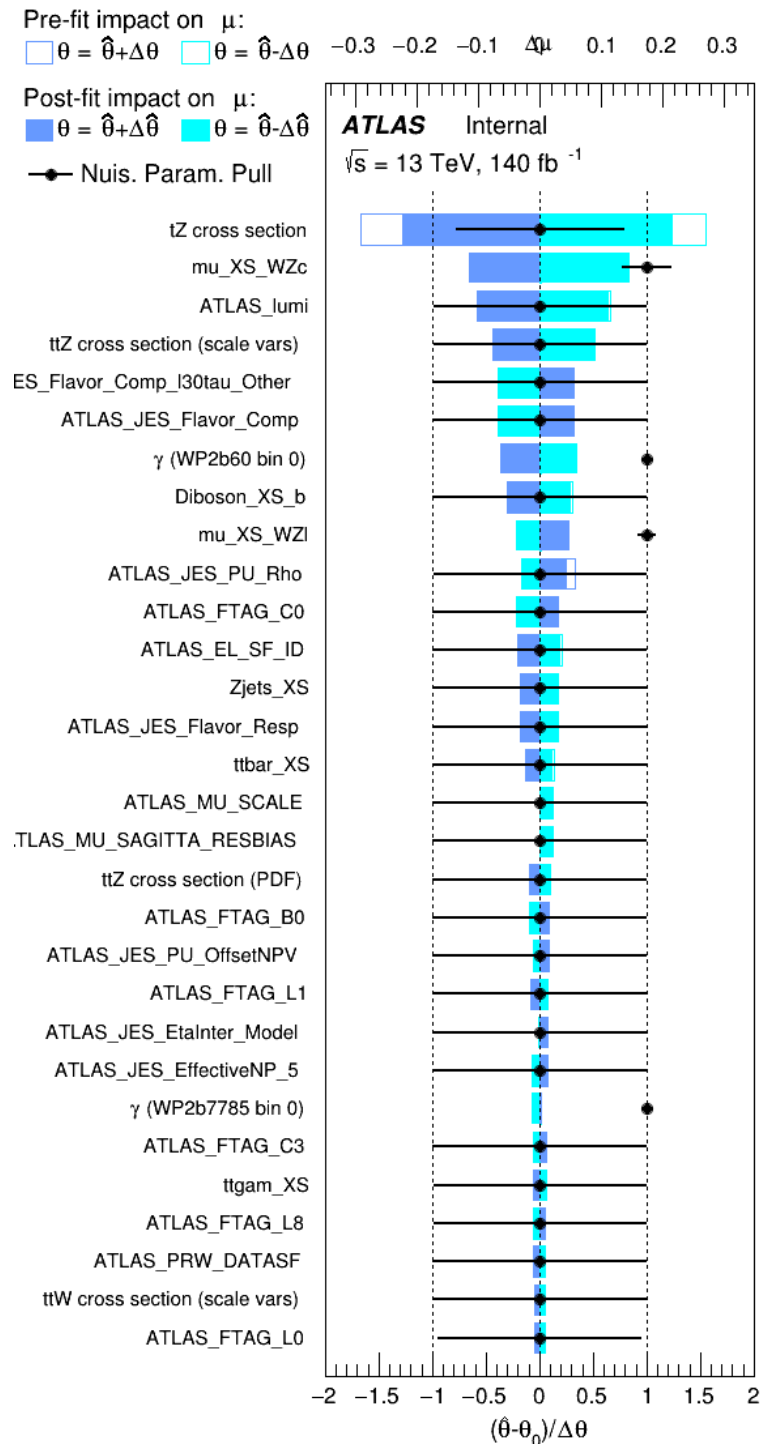


Figure 33: Impact of systematic uncertainties on the signal-strength of $WZ + b$ in 2-jet events.

447 The large impact of the Jet Energy Scale and Jet Flavor Tagging is unsurprising, as the shape
 448 of the fit regions depends heavily on the modeling of the jets. The other major sources of
 449 uncertainty come from background modelling and cross-section uncertainty. The pie charts in
 450 figure 34 show that for the modelling uncertainties that contribute most correspond to the most
 451 significant backgrounds.

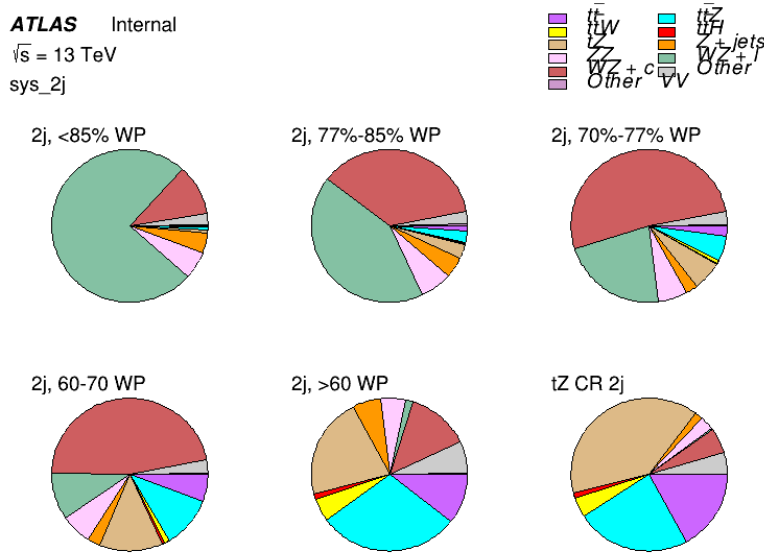


Figure 34: Post-fit background composition of the 2-jet fit regions.

452 The correlations between these nuisance parameters are summarized in figure 35.

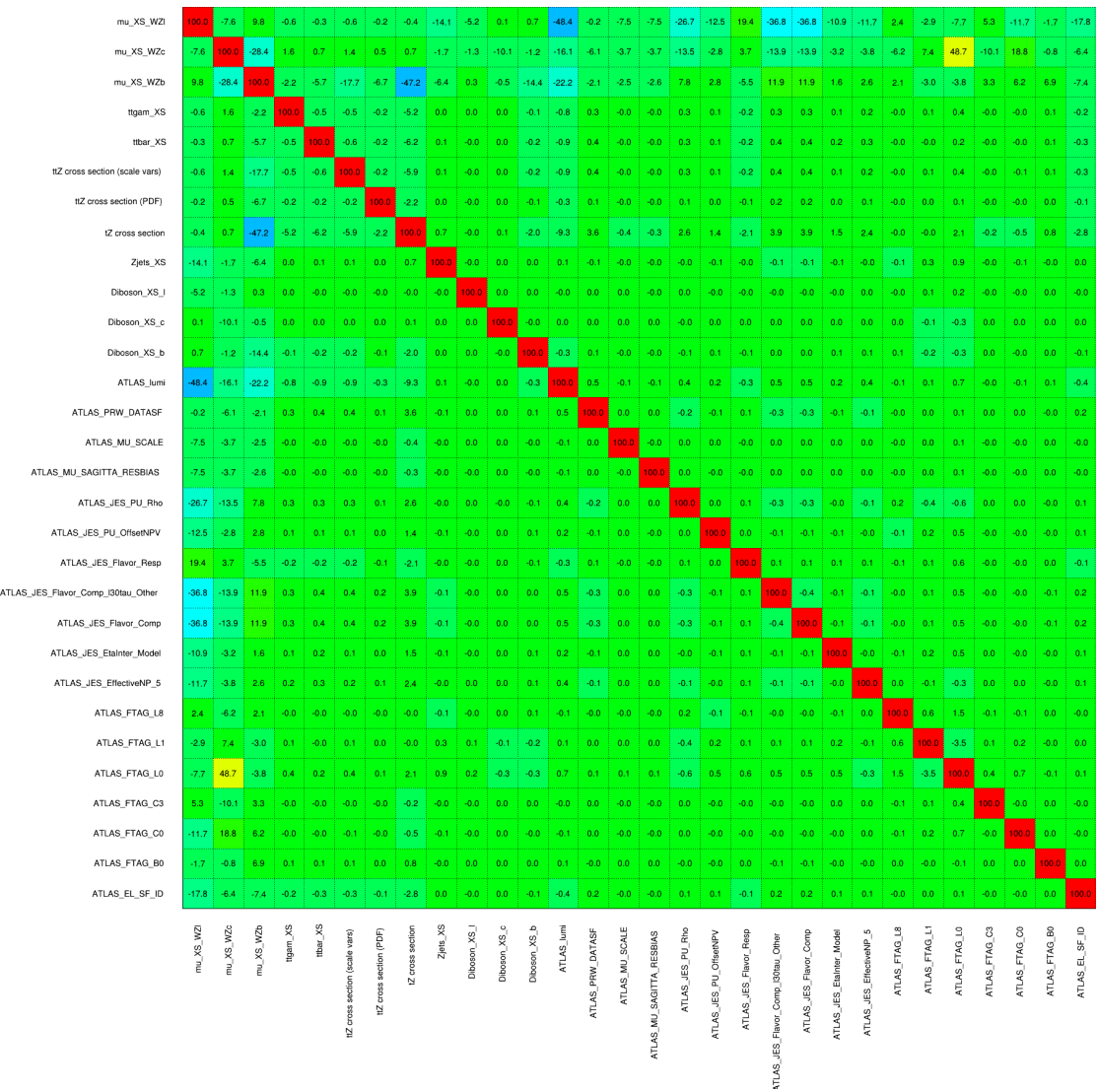


Figure 35: Correlations between nuisance parameters in the 2-jet fit

453 As in the 1-jet case, no significant, unexpected correlations are found between nuisance
 454 parameters.

9 Conclusion

456 A measurement of $WZ + \text{heavy flavor}$ is performed using 140 fb^{-1} of $\sqrt{s} = 13 \text{ TeV}$ proton-
 457 proton collision data collected by the ATLAS detector at the LHC. This section will be include

458 final results once unblinded.

459 **References**

- 460 [1] M. Aaboud et al. ‘Observation of electroweak $W^\pm Z$ boson pair production in association
461 with two jets in pp collisions at $\sqrt{s} = 13$ TeV with the ATLAS detector’. In: *Phys.
462 Lett.* B793 (2019), pp. 469–492. doi: [10.1016/j.physletb.2019.05.012](https://doi.org/10.1016/j.physletb.2019.05.012). arXiv:
463 [1812.09740 \[hep-ex\]](https://arxiv.org/abs/1812.09740).
- 464 [2] T. Gleisberg et al. ‘Event generation with SHERPA 1.1’. In: *JHEP* 02 (2009), p. 007. doi:
465 [10.1088/1126-6708/2009/02/007](https://doi.org/10.1088/1126-6708/2009/02/007). arXiv: [0811.4622 \[hep-ph\]](https://arxiv.org/abs/0811.4622).
- 466 [3] ATLAS Collaboration. *Electron efficiency measurements with the ATLAS detector using
467 the 2015 LHC proton–proton collision data*. ATLAS-CONF-2016-024. 2016. URL: <https://cds.cern.ch/record/2157687>.
- 468 [4] ATLAS Collaboration. ‘Measurement of the muon reconstruction performance of the
469 ATLAS detector using 2011 and 2012 LHC proton–proton collision data’. In: *Eur. Phys.
470 J. C* 74 (2014), p. 3130. doi: [10.1140/epjc/s10052-014-3130-x](https://doi.org/10.1140/epjc/s10052-014-3130-x). arXiv: [1407.3935
471 \[hep-ex\]](https://arxiv.org/abs/1407.3935).
- 472 [5] *Evidence for the associated production of the Higgs boson and a top quark pair with the
473 ATLAS detector*. Tech. rep. ATLAS-CONF-2017-077. Geneva: CERN, Nov. 2017. URL:
474 <https://cds.cern.ch/record/2291405>.
- 475 [6] ATLAS Collaboration. *Jet Calibration and Systematic Uncertainties for Jets Reconstructed
476 in the ATLAS Detector at $\sqrt{s} = 13$ TeV*. ATL-PHYS-PUB-2015-015. 2015. URL:
477 <https://cds.cern.ch/record/2037613>.
- 478 [7] ATLAS Collaboration. *Selection of jets produced in 13 TeV proton–proton collisions with
479 the ATLAS detector*. ATLAS-CONF-2015-029. 2015. URL: [https://cds.cern.ch/
480 record/2037702](https://cds.cern.ch/record/2037702).
- 481 [8] ATLAS Collaboration. ‘Performance of pile-up mitigation techniques for jets in pp col-
482 lisions at $\sqrt{s} = 8$ TeV using the ATLAS detector’. In: *Eur. Phys. J. C* 76 (2016), p. 581.
483 doi: [10.1140/epjc/s10052-016-4395-z](https://doi.org/10.1140/epjc/s10052-016-4395-z). arXiv: [1510.03823 \[hep-ex\]](https://arxiv.org/abs/1510.03823).
- 484 [9] ATLAS Collaboration. *Performance of missing transverse momentum reconstruction with
485 the ATLAS detector in the first proton–proton collisions at $\sqrt{s} = 13$ TeV*. ATL-PHYS-
486 PUB-2015-027. 2015. URL: <https://cds.cern.ch/record/2037904>.
- 487 [10] P. S. A. Hoecker. ‘TMVA 4 Toolkit for Multivariate Data Analysis with ROOT’. In:
488 *arXiv:physics/0703039* (2013).
- 489 [11] F. Cardillo et al. ‘Measurement of the fiducial and differential cross-section of a top quark
490 pair in association with a Z boson at 13 TeV with the ATLAS detector’. In: ATL-COM-
491 PHYS-2019-334 (Apr. 2019). URL: <https://cds.cern.ch/record/2672207>.

- 493 [12] ATLAS Collaboration. ‘Luminosity determination in pp collisions at $\sqrt{s} = 7$ TeV using
494 the ATLAS detector at the LHC’. In: *Eur. Phys. J. C* 71 (2011), p. 1630. doi: [10.1140/epjc/s10052-011-1630-5](https://doi.org/10.1140/epjc/s10052-011-1630-5). arXiv: [1101.2185 \[hep-ex\]](https://arxiv.org/abs/1101.2185).
- 496 [13] G. Aad et al. ‘Jet energy resolution in proton-proton collisions at $\sqrt{s} = 7$ TeV recorded
497 in 2010 with the ATLAS detector’. In: *The European Physical Journal C* 73.3 (Mar.
498 2013), p. 2306. issn: 1434-6052. doi: [10.1140/epjc/s10052-013-2306-0](https://doi.org/10.1140/epjc/s10052-013-2306-0). URL:
499 <https://doi.org/10.1140/epjc/s10052-013-2306-0>.
- 500 [14] A. Collaboration. ‘Performance of b -jet identification in the ATLAS experiment’. In:
501 *Journal of Instrumentation* 11.04 (2016), P04008. URL: <http://stacks.iop.org/1748-0221/11/i=04/a=P04008>.